Identification of elastic properties of interphase and interface in graphene-polymer nanocomposites by atomistic simulations

Xiaoxin Lu, Fabrice Detrez, Julien Yvonnet, Jinbo Bai

Identification of elastic properties of interphase and interface in graphene-polymer nanocomposites by atomistic simulations

Xiaoxin Lu[a], Fabrice Detrez[b,*], Julien Yvonnet[b], Jinbo Bai[c]

[a] *Shenzhen Institute of advanced electronic materials, Shenzhen Institutes of Advanced Technology, Chinese Academy of Sciences, Shenzhen 518103, P.R.China*
[b] *MSME, Univ Gustave Eiffel, CNRS UMR 8208, Univ Paris Est Creteil, F-77454 Marne-la-Vallée, France*
[c] *Université Paris-Saclay, CentraleSupélec, CNRS, Laboratoire de Mécanique des Sols, Structures et Matériaux (MSSMAT), 91190, Gif-sur-Yvette, France*

Abstract

This article tackles the problem of identification of elastic continuum model by atomistic simulations for graphene polymer nanocomposite. The Atomistic Local IdentificAtion of Stiffness method, so-called ALIAS method, is developed to estimate the local stiffness tensor at all points of polymer graphene laminate nanocomposite. Results suggest that the graphene can be modeled at continuum scale by a general imperfect interface with zero thickness. Moreover, the identification procedure reveals the existence of interphase on either side of the graphene with a thickness of 1 nm, which is one and a half times stiffer than the polymer bulk matrix. The identified continuum model is used to study the effective elastic properties of nanocomposites with sandwich microstructure. This study at continuum scale reveals a softening effect due the very low stiffness of slip along graphene plane. The softening due to the interfaces is preponderant in relation to the interphase stiffening. Finally, the continuum model also suggests that the wrinkling of graphene increases the stiffness of nanocomposites.

Keywords: Polymer nanocomposites, Graphene, Interface, Interphase, Mechanical properties

1. Introduction

Graphene, as one of the stiffest known materials, whose Young's modulus is around 1 TPa [1, 2], is an attractive candidate for use in high-performance polymer-based nanocomposites. From 2000s, a significant amount of research has been carried out on graphene nano-platelets (GNP) or graphene-derived materials based polymer nanocomposites due to their potential for large increases in toughness, strength and stiffness [3, 4, 5, 6]. The enhanced mechanical properties of the nanocomposites have been found to depend on various factors including the GNP-polymer bonding, the concentration and dispersion of GNP, the defects in GNP [7, 8, 9]. Many experimental studies have shown that the GNP polymer interface and the interphase region greatly influence the effective mechanical properties of the nanocomposites (see, e.g. [10, 11, 12]). In this paper, the polymer close to GNP filler is called interphase and the term interface indicates a discontinuity surface, which is generally located between two materials.

The existence and the influence of interfaces and interphases have been experimentally observed in GNP polymer nanocomposites [13, 14, 15]. They have been theoretically demonstrated in polymer nanocomposites by atomistic simulations [16, 17, 18, 19, 20]. However, their respective roles on elastic behavior are not yet well understood. So, it is necessary to have an identification procedure which is able to decouple the elastic contributions of interfaces and interphases. This is hardly accessible through an inverse analysis based on atomistic simulations or experimental data because the effects of interfaces and interphases can be hardly distinguished. The objective of this paper is to propose an identification methodology of elastic

*Corresponding author *Email: fabrice.detrez@univ-eiffel.fr*

models with interphases and/or imperfect interfaces in GNP polymer nanocomposites. Possible applications of these continuum models could be the definition of a finite element framework taking into account the size effects to study at mesoscale the concentration and dispersion of GNP on elastic properties (see, e.g. [21, 22, 23, 24, 25] for similar studies on electric and thermal conductivity properties). We will restrict our study to a sandwich structure model of nanocomposite (see Figure 2) for reasons of clarity.

The strong influence of interfaces and interphases induces size effects on the mechanical behavior. These size effects have been observed in several polymer nanocomposites (see, e.g. [26, 27] for a review). There are mainly two families of continuum models in the literature able to capture size effects: the models with an interphase surrounding inclusions and the imperfect interface models. The first class of models with interphases have been used on polymer nanocomposites for mean-field homogenization (see, e.g. [28, 29]) and for numerical homogenization [21]. The mechanical studies using an interphase region in polymer carbon nanocomposites were mostly performed on the polymer reinforced with carbon nanotubes [30, 31, 32, 33, 34, 35]. Atomistic simulations are also performed to identify the interphase elastic parameter by inverse analysis to reproduce the size effect [36, 37, 38, 39]. In these studies, the interphase is assumed isotropic and the elastic parameters are fited to reproduce the experimental or atomistic simulation data. The study of interphase anisotropy is very delicate through inverse analysis. The second class of models that incorporates zero-thickness imperfect interfaces [40, 41, 42, 43] is also able to capture the size effects [44, 45]. The general imperfect interfaces combine the discontinuity of displacement of cohesive zone model [46, 47] and the discontinuity of the traction vector of the membrane-type interface model [48, 49]. To the best of our knowledge, although the atomistic simulations are widely used to identity the physical effective parameters of the materials such as Young's modulus, glass transition parameter, etc.[50, 51], the atomistic identification of the anisotropic local materials parameters remains an open question. Nevertheless, special cases of imperfect interfaces have identified by atomistic simulations, such as membrane-type interface in thin material [52, 53, 54, 55, 56, 57, 58, 59]; and cohesive zone model to the study of the decohesion between filler and matrix in polymer nanocompoistes [24, 60, 61, 62, 63, 64, 65, 66]. Note that some authors performed atomistic simulations to study the cohesion between carbon filler and polymer matrix without identifying the cohesive zone model [17, 18, 67, 68, 69, 70].

We introduce the methodology of Atomistic Local IdentificAtion of Stiffness, called in this paper ALIAS methodology, and which allows to establish an equivalent continuum model from an atomistic model. It consists of measuring the local stress and strain fields under different deformations of the simulation box and then deducing the elastic tensor fields. The novel possibilities offered by the ALIAS methodology are the identification of a continuum model allowing to take into account size effects from an unique size box of atomistic model, and also the characterization of interphase anisotropy. The ALIAS methodology is a sequential multiscale approach following the classification proposed in the comprehensive book of [71]. The other category of atomistic-continuum coupling approaches is the concurrent method (see, e.g. [71, 72] for an overview) and the application to polymer material [73, 74, 75]. Although they contain more physical ingredients, the main drawback for GNP nanocomposite applications is the GNP number in a Representative Volume Element (RVE) that induces a large number of atomistic domains, leading to untractable computational times. However, the ALIAS method is inspired by concurrent methods in the sense that they are based on the same two key features: the collection of continuum information from atomic level and the constraint of atomistic simulations to impose the continuum field. For the first point, the Murdoch-Hardy procedure [76] is used because it allows to define both the velocity field and the stress field at all points. Regarding the second point, the Cauchy-Born rule [77, 78] is the fundamental assumption to link the continuum strain to the atom displacement. It is suitable for the multiscale coupling of bulk materials such as crystalline materials [see, e.g. 79, 80]. However, for the amorphous materials such as glass or polymer, it is no longer applicable [81, 82, 83, 84, 85]. To overcome this difficulty, we impose the deformation to the atomic simulation box and we compute the atoms displacement by the Athermal, Quasistatic Simulations algorithm introduced by [86, 87, 88] and used to determined the elastic constants of amorphous glasses materials by [81, 82, 83, 84, 85]. The novelty of ALIAS method is the estimation of the local displacement field during simulations for a given macroscopic strain imposed to the atomistic simulation box. This, allows us to deduce the strain fields and the stiffness tensor at each point.

The paper is organized as follows. First, in section 2, a short overview of the general imperfect interface

framework is established. In section 3, we describe the atomistic model, the ALIAS methodology and their results. Finally, in section 4, we discuss the influence of interphase and interface on elastic properties of sandwich graphene/polymer nano-composite.

Notations and definitions

Notations are based on the following conventions. Scalars are in italics lowercase (a), vectors are bold-face in lowercase ($\mathbf{a}$), second-order tensors are bold-face in uppercase or bold-face in greek symbol ($\mathbf{A}, \boldsymbol{\alpha}$), and fourth-order tensors are blackboard bold in uppercase ($\mathbb{A}$). The dyadic product of two vectors $\mathbf{a}$ and $\mathbf{b}$ is a second-order tensor $\mathbf{D} = \mathbf{a} \otimes \mathbf{b}$ with $(D)_{ij} = (a)_i (b)_j$. The scalar product of two vectors $\mathbf{a}$ and $\mathbf{b}$ is denoted $\mathbf{a} \cdot \mathbf{b} = (a)_i (b)_i$. The scalar product of two second-order tensors $\mathbf{A}$ and $\mathbf{B}$ is denoted $\mathbf{A} : \mathbf{B} = (A)_{ij} (B)_{ij}$. Quantities defined on the interface are distinguished from those in the bulk by a super-script $(\bullet)^s$. The continuum fields identified by the ALIAS methodology are designated by a sub-script $(\bullet)_w$ Moreover, macroscale quantities and effective quantities are differentiated from microscale quantities by a bar placed above the quantity $(\bar{\bullet})$. The jump of a quantity $(\bullet)$ over the interface $\mathcal{I}$ are defined by $[\![\bullet]\!] = \bullet|_{\mathcal{I}}^{+} - \bullet|_{\mathcal{I}}^{-}$. The list of symbols used in this paper is provided in Table 1.

Table 1: Symbols table

L_x, L_y, L_z	Side length of the RVE
t_I	Thickness of interphase
$\mathbf{n}_{\mathcal{I}}$	Unit normal vector to the interface $\mathcal{I}$
ϕ and ϕ^s	Bulk/interfacial free energy density
$\mathbf{u}(\mathbf{x})$, $\mathbf{u}^s(\mathbf{x})$	Displacement field and surfacic displacement field in interface $\mathcal{I}$
$[\![\mathbf{u}]\!]$	Displacement jump across the interface $\mathcal{I}$
$\mathbf{t}^s$, $[\![\mathbf{t}]\!]$	Average traction vector and traction vector jump across the interface $\mathcal{I}$
$\boldsymbol{\epsilon}(\mathbf{x})$, $\boldsymbol{\epsilon}^s(\mathbf{x})$	Infinitesimal strain tensor and infinitesimal surface strain tensor in interface
$\boldsymbol{\sigma}(\mathbf{x})$, $\boldsymbol{\sigma}^s(\mathbf{x})$	Cauchy stress tensor in the bulk and surface Cauchy stress tensor in interface
$\mathbb{C}^b$, $\mathbb{C}^I$	The fourth-order symmetric stiffness tensor for bulk polymer and interphase
$\mathbb{C}^s$	The fourth-order symmetric interfacial stiffness tensors
$\mathbf{K}^s$	Second-order symmetric cohesive interfacial stiffness tensor
$\bar{\boldsymbol{\epsilon}}$, $\bar{\boldsymbol{\sigma}}$	Effective infinitesimal strain tensor and effective Cauchy stress tensor
$\overline{\mathbb{C}}_C$, $\overline{\mathbb{C}}_A$	Effective stiffness tensor compute by continuum model and by atomistic model
$\mathfrak{m}_\alpha$	Masse of αth atom
$\mathbf{r}_\alpha$, $\mathbf{r}_\alpha^{(0)}$	Current and initial position of αth atom
$r_{\alpha\beta}$, $\mathbf{n}_{\alpha\beta}$	Inter-atomic distance and covalent bond direction between αth atom and βth atom
$\mathfrak{v}_\alpha$	Velocity of αth atom
$\mathbf{f}_{\alpha\beta}$, $\mathbf{f}_\alpha = \sum_\beta \mathbf{f}_{\alpha\beta}$	Force of βth atom on the αth atom and force on αth atom
$\mathcal{U}(\{\mathbf{r}_\alpha\}, \bar{\boldsymbol{\epsilon}})$	Potential energy of atomistic system for prescribe macro strain $\bar{\boldsymbol{\epsilon}}$
$w(\mathbf{x})$, $b_w(\mathbf{x}, \mathbf{r}_\alpha, \mathbf{r}_\beta)$	Weight function and bond function Murdoch-Hardy procedure
$\rho_w(\mathbf{x})$	Atomistic mass density at point $\mathbf{x}$
$\mathbf{u}_w^{(E)}(\mathbf{x})$, $\mathbf{v}_w(\mathbf{x})$	Atomistic Eulerian displacement and atomistic velocity fields at point $\mathbf{x}$
$\boldsymbol{\sigma}_w(\mathbf{x})$, $\boldsymbol{\epsilon}_w(\mathbf{x})$	Atomistic Cauchy stress tensor and atomistic strain tensor at point $\mathbf{x}$
$\mathbb{C}_w(\mathbf{x})$	Atomistic stiffness tensor at point $\mathbf{x}$
$s_w(\mathbf{x})$	Nematic order parameter at point $\mathbf{x}$

2. Generalized imperfect interface framework

The purpose of this section is to establish the equations governing continua embedding general interface elastic model. A comprehensive description of this model can be found for the case of infinitesimal displacements in [45] and for its extension to finite deformation in [89, 90]. In this section, we assume infinitesimal

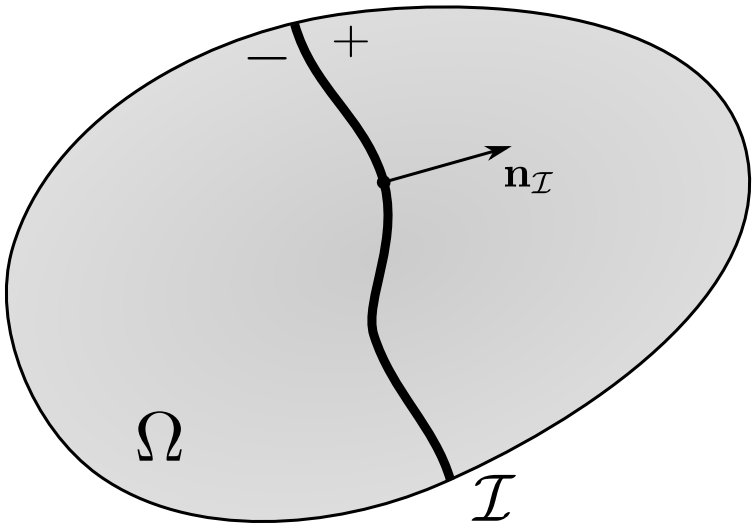

Figure 1: Sketch of domains Ω with the imperfect interface $\mathcal{I}$ and the unit normal $\mathbf{n}_{\mathcal{I}}$.

displacements and linear behavior for the sake of simplicity. The interface $\mathcal{I}$ splits the body Ω into two regions (see Figure 1). The unit normal of the interface $\mathcal{I}$ is denoted by $\mathbf{n}_{\mathcal{I}}$.

The displacement in the body is denoted by $\mathbf{u}(\mathbf{x})$ and the displacement jump, $[\![\mathbf{u}]\!]$, across the interface $\mathcal{I}$ is defined by

$$[\![\mathbf{u}]\!] = \mathbf{u}|_{\mathcal{I}}^{+} - \mathbf{u}|_{\mathcal{I}}^{-}, \tag{1}$$

where $\mathbf{u}|_{\mathcal{I}}^{+}$ and $\mathbf{u}|_{\mathcal{I}}^{-}$ are the values of displacement in the upper and lower surfaces of interface $\mathcal{I}$ respectively.

The displacement field, $\mathbf{u}^s$, inside the interface $\mathcal{I}$ is defined as the median value according to:

$$\mathbf{u}^s(\mathbf{x}) = \frac{1}{2}\left(\mathbf{u}|_{\mathcal{I}}^{+} + \mathbf{u}|_{\mathcal{I}}^{-}\right), \qquad \forall \mathbf{x} \in \mathcal{I}. \tag{2}$$

The infinitesimal strain tensor in the bulk is defined by

$$\boldsymbol{\epsilon}(\mathbf{x}) = \frac{1}{2}\left(\nabla \mathbf{u}(\mathbf{x}) + \nabla \mathbf{u}^T(\mathbf{x})\right), \qquad \forall \mathbf{x} \in \Omega, \tag{3}$$

and the infinitesimal strain tensor on the interface is defined by

$$\boldsymbol{\epsilon}^s(\mathbf{x}) = \frac{1}{2}\left(\nabla^s \mathbf{u}^s(\mathbf{x}) + (\nabla^s \mathbf{u}^s(\mathbf{x}))^T\right), \qquad \forall \mathbf{x} \in \mathcal{I}, \tag{4}$$

where ∇ is the gradient operator, $\nabla^s = \mathbf{P} \cdot \nabla$ is the interface gradient operator and $\mathbf{P} = \mathbf{I} - \mathbf{n}_{\mathcal{I}} \otimes \mathbf{n}_{\mathcal{I}}$ is the projector onto the tangent plane of the interface $\mathcal{I}$.

In absence of external force densities in bulk and in the interface, the balance equations are given by:

$$\nabla \cdot \boldsymbol{\sigma} = \mathbf{0} \qquad \forall \mathbf{x} \in \Omega, \tag{5}$$

$$\nabla^s \cdot \boldsymbol{\sigma}^s + [\![\mathbf{t}]\!] = \mathbf{0} \qquad \forall \mathbf{x} \in \mathcal{I}, \tag{6}$$

where $\nabla \cdot$ is the divergence operator; $\nabla^s \cdot \{\cdot\} = \nabla \cdot \{\cdot\} : \mathbf{P}$ is the interface divergence operator; $\boldsymbol{\sigma}^s$ the interfacial stress and $[\![\mathbf{t}]\!]$ is the traction vector jump across the interface defined by

$$[\![\mathbf{t}]\!] = [\![\boldsymbol{\sigma} \cdot \mathbf{n}_{\mathcal{I}}]\!] = \left(\boldsymbol{\sigma}|_{\mathcal{I}}^{+} - \boldsymbol{\sigma}|_{\mathcal{I}}^{-}\right) \cdot \mathbf{n}_{\mathcal{I}}. \tag{7}$$

We assume the existence of a bulk free energy density $\phi(\boldsymbol{\epsilon})$ and an interfacial free energy density

$\phi^s(\boldsymbol{\epsilon}^s, [\![\mathbf{u}]\!])$ in the bulk and the interface respectively, such as the behavior laws derive from them

$$\boldsymbol{\sigma} = \partial_{\boldsymbol{\epsilon}}\phi \qquad \forall \mathbf{x} \in \Omega, \tag{8}$$

$$\boldsymbol{\sigma}^s = \partial_{\boldsymbol{\epsilon}^s}\phi^s \qquad \forall \mathbf{x} \in \mathcal{I}, \tag{9}$$

$$\mathbf{t}^s = \partial_{[\![\mathbf{u}]\!]}\phi^s \qquad \forall \mathbf{x} \in \mathcal{I}, \tag{10}$$

where $\mathbf{t}^s$ denotes the average traction across the interface, defined by

$$\mathbf{t}^s = \frac{1}{2}\left(\boldsymbol{\sigma}|_{\mathcal{I}}^{+} + \boldsymbol{\sigma}|_{\mathcal{I}}^{-}\right) \cdot \mathbf{n}_{\mathcal{I}}. \tag{11}$$

Under the assumptions of standard linear elastic behavior with internal stresses, both free energies are given by

$$\phi(\boldsymbol{\epsilon}) = \frac{1}{2}\boldsymbol{\epsilon} : \mathbb{C}(\mathbf{x}) : \boldsymbol{\epsilon} + \boldsymbol{\tau}(\mathbf{x}) : \boldsymbol{\epsilon} + \phi_0 \qquad \forall \mathbf{x} \in \Omega, \tag{12}$$

$$\phi^s(\boldsymbol{\epsilon}^s, [\![\mathbf{u}]\!]) = \frac{1}{2}\boldsymbol{\epsilon}^s : \mathbb{C}^s(\mathbf{x}) : \boldsymbol{\epsilon}^s + \boldsymbol{\tau}^s(\mathbf{x}) : \boldsymbol{\epsilon}^s + \frac{1}{2}[\![\mathbf{u}]\!].\mathbf{K}^s(\mathbf{x}).[\![\mathbf{u}]\!] + \phi_0^s \qquad \forall \mathbf{x} \in \mathcal{I}, \tag{13}$$

where $\mathbb{C}(\mathbf{x})$ is the fourth-order symmetric bulk stiffness tensor; $\mathbb{C}^s(\mathbf{x})$ is the fourth-order symmetric interfacial stiffness tensors; $\boldsymbol{\tau}$ is the internal stresses in the bulk and $\boldsymbol{\tau}^s$ is the internal surface stress; ϕ_0 and ϕ_0^s are the free energies of bulk and interface under zero strain and zero jump displacement; and $\mathbf{K}^s$ is the second-order symmetric tensor which corresponds to the cohesive stiffness of interface.

3. Identification of continuum elastic parameters by atomistic simulations

3.1. Atomistic model

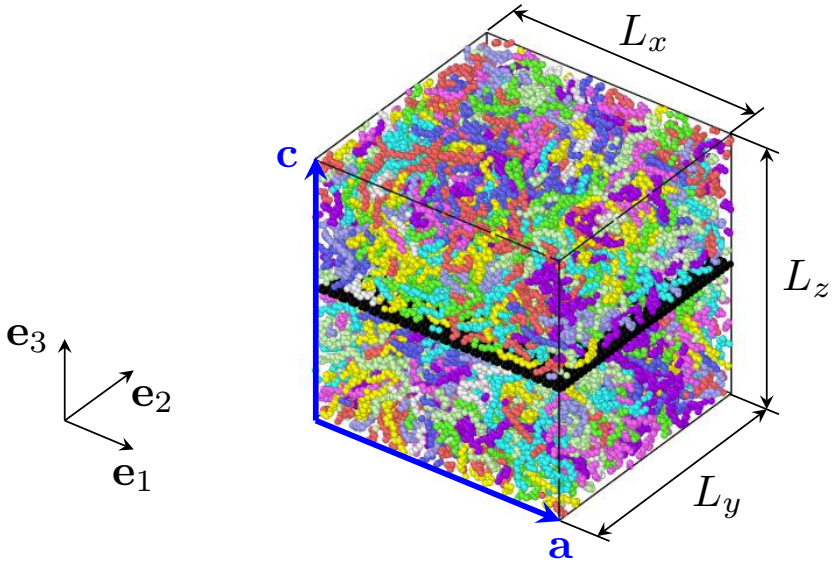

Figure 2: Graphene polymer nanocomposite with sandwich structure under periodical boundary condition, single layer graphene is located in the middle of the box.

At the atomic scale, the graphene polymer nanocomposite is modeled by a set of N classical interacticting point particules with sandwich structure in a rectangular box under periodic boundary condition (see Figure 2). Two types of particles are considered: the carbon in the graphene sheet and the $-CH_2-$ atom group

in polymer chains. Each macromolecular chain contains 500 $-CH_2-$ units. The length and the width of the box are given by $L_x = 100.8\mathring{A}$ and $L_y = 94.57\mathring{A}$. The box contains 25×38 crystal lattice in graphene sheet. The thickness L_z depends on the polymer chain number. The shape of the parallelepiped simulation box is represented by a set of 3 vectors $\mathbf{a}, \mathbf{b}, \mathbf{c}$ through the second order tensor $\mathbf{h} = (\mathbf{a}, \mathbf{b}, \mathbf{c})$. The initial system is prepared from the off-lattice self-avoiding random walk combining the simultaneously molecular dynamics relaxation [91]. We assume that the particles interact through the DREIDING potential energy function [92], where the electrostatic contributions are neglected for simplicity reasons. The potential energy $\mathcal{U}\left(\{\mathbf{r}_\alpha\}, \bar{\boldsymbol{\epsilon}}\right)$, depends on the current position of particles, $\{\mathbf{r}_\alpha\}$, via the DREIDING potential as well as on the shape of simulation box via the effective infinitesimal strain tensor $\bar{\boldsymbol{\epsilon}}$ of the box defined by

$$\bar{\boldsymbol{\epsilon}} = \frac{1}{2}\left(\mathbf{F} + \mathbf{F}^T\right) - \mathbf{I}, \quad \text{where} \quad \mathbf{F} = \mathbf{h} \cdot \left(\mathbf{h}^{(0)}\right)^{-1}, \tag{14}$$

$\mathbf{I}$ is the unit second order tensor and $\mathbf{h}^{(0)}$ defines the shape of the parallelepiped simulation box in the initial reference configuration ($\bar{\boldsymbol{\epsilon}} = \mathbf{0}$).

In our study, we suppose that the tensor $\mathbf{h}(t)$ is parameterized by a scalar t called pseudo time. We assume that the system follows an equilibrium trajectory, even though the actual potential energy $\mathcal{U}\left(\{\mathbf{r}_\alpha\}, \bar{\boldsymbol{\epsilon}}(t)\right)$ is in a local minimum. The Athermal, Quasistatic Simulations algorithm is used to ensure that the system follows an equilibrium trajectory. This simulation technics have been introduced by [86, 87, 88] and used to determine the elastic constants of amorphous glasses materials by [81, 82, 83, 84, 85]. For each small pseudo time increment, δt, this algorithm consists of moving affinely the atoms from previous state, and then to perform a minimization to find the nearest local minimum.

The velocity of α-th atom is estimated by backward finite difference approximation

$$\mathbf{v}_\alpha(t) \approx \frac{\mathbf{r}_\alpha(t) - \mathbf{r}_\alpha(t - \delta t)}{\delta t}. \tag{15}$$

It is interesting to note that the velocity tends to zero in the quasistatic limit (i.e. $\mathbf{v}_\alpha \to \mathbf{0}$ and $\delta t \to \infty$), therefore we could neglect it in most of cases. However, the atom velocity atomic is necessary to define the displacement field.

The equilibrium trajectory imposes that the force on particle α is always zero

$$\mathbf{f}_\alpha = -\partial_{\mathbf{r}_\alpha}\mathcal{U}\left(\{\mathbf{r}_\alpha\}, \bar{\boldsymbol{\epsilon}}(t)\right) = \sum_{\beta \neq \alpha} \mathbf{f}_{\alpha\beta} = 0. \tag{16}$$

Here $\mathbf{f}_{\alpha\beta}$ is the force of β-th atom on the α-th atom. Since the potentials used are conservative, they can be expressed in terms of set of inter-atomic distances $r_{\alpha\beta}$ between the α-th and β-th atoms [71, 93]. Consequently, a set of central forces between the pairs of atoms $\mathbf{f}_{\alpha\beta}$ can be defined by

$$\mathbf{f}_{\alpha\beta} = -\partial_{r_{\alpha\beta}}\mathcal{U}\left(\{\mathbf{r}_\alpha\}, \bar{\boldsymbol{\epsilon}}(t)\right)\frac{\mathbf{r}_\alpha - \mathbf{r}_\beta}{r_{\alpha\beta}}. \tag{17}$$

The expressions of DREIDING potential in term of interatomic distances is given in supplementary information. It is interesting to note that this definition ensures that

$$\mathbf{f}_{\alpha\beta} = -\mathbf{f}_{\beta\alpha}, \qquad \text{and} \qquad \mathbf{f}_\alpha = \sum_{\beta \neq \alpha} \mathbf{f}_{\alpha\beta}. \tag{18}$$

3.2. Atomistic Local IdentificAtion of Stiffness: ALIAS methodology

The ALIAS methodology is based on the measurement of continuum stress and strain tensors for several imposed effective infinitesimal strain tensors $\bar{\boldsymbol{\epsilon}}$. The number of imposed effective infinitesimal strain tensors is chosen to explore a necessary set of strain-stress combinations to defined the stiffness fields. The Murdoch-Hardy procedure [76] is used to measure the continuum velocity and Cauchy's stress tensor fields from

atomistic quantities. In this paper, the continuum displacement field that allows to compute the strain field is obtained by integration of the velocity field.

3.2.1. Murdoch-Hardy procedure

The main point here is to identify the Eulerian specification of continuum fields, such as mass density, Cauchy's stress tensor and velocity, with local space averages of atomistic quantities, such as atom mass, atom velocity and interatomic forces. A physical interpretation of the Murdoch-Hardy procedure is that a device with a finite size measures the conservative quantities of interest at a point $\mathbf{x}$. This device is modeled by a scalar-valued weighting function $w(\mathbf{x})$ which defines a spatial averaging and satisfies the normalization condition

$$\int_{\mathbb{R}^3} w\left(\mathbf{x}\right) d\mathbf{x} = 1. \tag{19}$$

The mass density $\rho_w\left(\mathbf{x},t\right)$ is defined as

$$\rho_w\left(\mathbf{x},t\right) = \sum_\alpha m_\alpha w\left(\mathbf{r}_\alpha\left(t\right) - \mathbf{x}\right). \tag{20}$$

Here, the mass density $\rho_w\left(\mathbf{x},t\right)$ must verify the continuity equation (conservation of mass) in the current configuration

$$\partial_t \rho_w + \nabla_{\mathbf{x}} \cdot \left(\rho_w \mathbf{v}_w\right) = 0, \tag{21}$$

where ∂_t and $\nabla_{\mathbf{x}} \cdot$ denote the partial derivative with respect to the time and the divergence operator with respect to the spatial coordinate $\mathbf{x}$, respectively.

To satisfy the continuity equation (21), the Eulerian specification of velocity fields $\mathbf{v}_w(\mathbf{x},t)$ is defined by [see e.g. 76]

$$\mathbf{v}_w\left(\mathbf{x},t\right) = \begin{cases} \frac{1}{\rho_w}\sum_\alpha m_\alpha \mathfrak{v}_\alpha\left(t\right) w\left(\mathbf{r}_\alpha\left(t\right) - \mathbf{x}\right) & \text{if } \rho_w\left(\mathbf{x},t\right) \neq 0 \\ \mathbf{0} & \text{otherwise} \end{cases}. \tag{22}$$

Following [93, 94, 95], the atomistic Cauchy stress tensor is decomposed in two terms: the kinematics contribution, $\boldsymbol{\sigma}_{w,k}$, and the potential contribution, $\boldsymbol{\sigma}_{w,v}$, such as

$$\boldsymbol{\sigma}_w\left(\mathbf{x},t\right) = \boldsymbol{\sigma}_{w,k}\left(\mathbf{x},t\right) + \boldsymbol{\sigma}_{w,v}\left(\mathbf{x},t\right), \tag{23}$$

where

$$\boldsymbol{\sigma}_{w,k}\left(\mathbf{x},t\right) = -\sum_\alpha \left(\mathfrak{v}_\alpha\left(t\right) - \mathbf{v}_w\left(\mathbf{x},t\right)\right) \otimes \left(\mathfrak{v}_\alpha\left(t\right) - \mathbf{v}_w\left(\mathbf{x},t\right)\right) w\left(\mathbf{r}_\alpha\left(t\right) - \mathbf{x}\right). \tag{24}$$

Here, the kinematics contribution of the atomistic Cauchy stress tensor and the velocity fields are assumed to be negligible under the quasistatic assumption ($\delta t \to \infty$), i.e. $\mathfrak{v}_\alpha \propto (\delta t)^{-1} \to \mathbf{0}$ for all α, t implying $\mathbf{v}_w(\mathbf{x},t) \propto (\delta t)^{-1} \to \mathbf{0}$ and $\boldsymbol{\sigma}_{w,k}\left(\mathbf{x},t\right) \propto (\delta t)^{-2} \to \mathbf{0}$ for all $\mathbf{x}$, t.

The potential contribution of atomistic Cauchy stress, $\sigma_{w,v}$ satisfies the balance equation

$$\nabla_{\mathbf{x}} . \boldsymbol{\sigma}_{w,v}\left(\mathbf{x},t\right) = \sum_\alpha \mathbf{f}_\alpha\left(t\right) w\left(\mathbf{r}_\alpha\left(t\right) - \mathbf{x}\right). \tag{25}$$

The expression of $\boldsymbol{\sigma}_{w,v}$ is not unique, the most common one is

$$\boldsymbol{\sigma}_{w,v}\left(\mathbf{x},t\right) = \frac{1}{2}\sum_{\alpha,\beta} \mathbf{f}_{\alpha\beta}\left(t\right) \otimes \left(\mathbf{r}_\beta\left(t\right) - \mathbf{r}_\alpha\left(t\right)\right) b_w\left(\mathbf{x};\mathbf{r}_\alpha\left(t\right),\mathbf{r}_\beta\left(t\right)\right), \tag{26}$$

where $b_w\left(\mathbf{x},\mathbf{r}_\alpha\left(t\right),\mathbf{r}_\beta\left(t\right)\right)$ is the bond function expressed by

$$b_w\left(\mathbf{x};\mathbf{r}_\alpha\left(t\right),\mathbf{r}_\beta\left(t\right)\right) = \int_0^1 w((1-s)\mathbf{r}_\alpha + s\mathbf{r}_\beta - \mathbf{x})ds. \tag{27}$$

Note that the atomisitic definition of stress is not unique [71, 93, 94] and is a controversial topic in the literature [96].

3.2.2. Methotology of stiffness identification

First, we introduce a definition of the infinitesimal strain tensor field from the Mudoch-Hardy velocity field $\mathbf{v}_w(\mathbf{x},t)$ through the concept of the Eulerian displacement field. Following [97], we introduce the Eulerian displacement field, $\mathbf{u}_w^{(E)}(\mathbf{x},t)$, which allows to reconstruct the solid body as it was at the initial instant in an absolute referential before all transformations. The relation between the Eulerian displacement field and velocity fields is

$$\mathbf{v}_w(\mathbf{x},t) = -\frac{\mathrm{d}\mathbf{u}_w^{(E)}}{\mathrm{d}t}, \quad \text{or} \quad \partial_t \mathbf{u}_w^{(E)} = -\mathbf{v}_w.\left(\mathbf{I} + \nabla_{\mathbf{x}}\mathbf{u}_w^{(E)}\right), \tag{28}$$

where $\nabla_{\mathbf{x}}$ is the gradient operator with respect to the spatial coordinate $\mathbf{x}$. The Eulerian displacement field can be estimated by a finite difference approximation

$$\mathbf{u}_w^{(E)}(\mathbf{x},t+\delta t) \approx \mathbf{u}_w^{(E)}(\mathbf{x},t) - \delta t \mathbf{v}_w(\mathbf{x},t+\delta t) \cdot \left(\mathbf{I} + \nabla_{\mathbf{x}}\mathbf{u}_w^{(E)}(\mathbf{x},t)\right). \tag{29}$$

By introducing the definitions of the Eulerian specification of velocity fields $\mathbf{v}_w(\mathbf{x},t)$ (Eq. 22) combined with the definition of atomic velocities $\mathfrak{v}_\alpha(t)$ (Eq. 15), we can write the increment of the Eulerian displacement field :

$$\begin{aligned}
\Delta\mathbf{u}_w^{(E)}(\mathbf{x},t) &= \mathbf{u}_w^{(E)}(\mathbf{x},t+\delta t) - \mathbf{u}_w^{(E)}(\mathbf{x},t) \\
&= -\frac{\delta t}{\rho_w}\sum_\alpha m_\alpha \mathfrak{v}_\alpha(t)\, w(\mathbf{r}_\alpha(t)-\mathbf{x}) \cdot \left(\mathbf{I} + \nabla_{\mathbf{x}}\mathbf{u}_w^{(E)}(\mathbf{x},t)\right) \\
&= -\frac{1}{\rho_w}\sum_\alpha m_\alpha \left(\mathbf{r}_\alpha(t) - \mathbf{r}_\alpha(t-\delta t)\right) w(\mathbf{r}_\alpha(t)-\mathbf{x}) \cdot \left(\mathbf{I} + \nabla_{\mathbf{x}}\mathbf{u}_w^{(E)}(\mathbf{x},t)\right).
\end{aligned} \tag{30}$$

Note that the increment of Eulerian displacement field is independent of speudo time δt and that it is well defined in the quasistatic limit ($\delta t \to \infty$).

Under infinitesimal displacement assumption, the initial and final configuration can be considered as the same, therefore the classical displacement field $\mathbf{u}_w$ can be defined as the opposite of the Eulerian displacement field $\mathbf{u}_w = -\mathbf{u}_w^{(E)}(\mathbf{x})$. The infinitesimal strain tensor field $\boldsymbol{\epsilon}_w$ is defined by:

$$(\boldsymbol{\epsilon}_w)_{ij}(\mathbf{x}) = \frac{1}{2}\left(\partial_{x_i}(u_w)_j(\mathbf{x}) + \partial_{x_j}(u_w)_i(\mathbf{x})\right). \tag{31}$$

Here, we use a centered finite difference approximation of the spatial derivative of displacement field

$$\partial_{x_i}(u_w)_j(\mathbf{x}) \approx \frac{(u_w)_j(\mathbf{x}+\delta x\mathbf{e}_i) - (u_w)_j(\mathbf{x}-\delta x\mathbf{e}_i)}{2\delta x}. \tag{32}$$

The atomistic stiffness tensor $\mathbb{C}_w(\mathbf{x})$ at each point where the atomistic Cauchy's stress $\boldsymbol{\sigma}_w$ and the atomistic infinitesimal strain $\boldsymbol{\epsilon}_w$ are measured is defined by the least squares method, for a given set of K effective strain tensors $\bar{\boldsymbol{\epsilon}}^{(k)}$, such as

$$\mathbb{C}_w(\mathbf{x}) = \underset{\mathbb{C}_w(\mathbf{x})\in\mathbb{E}\mathrm{la}}{\operatorname{argmin}} \left\{ \sum_{k=1}^{K} \left\| \boldsymbol{\sigma}_w^{(k)}(\mathbf{x}) - \mathbb{C}_w(\mathbf{x}) : \boldsymbol{\epsilon}_w^{(k)}(\mathbf{x}) - \boldsymbol{\tau}_w(\mathbf{x}) \right\|_F^2 \right\} \tag{33}$$

where $\mathbb{E}\mathrm{la}$ is the set of fourth order elastic tensor with minor and major symmetry and $\|\boldsymbol{a}\|_F^2 = a_{ij}a_{ij}$ is the Frobenius norm associated to 2nd order tensor. Here $\boldsymbol{\sigma}_w^{(k)}(\mathbf{x})$ (resp. $\boldsymbol{\epsilon}_w^{(k)}(\mathbf{x})$) is the atomistic Cauchy's stress tensor (resp. the atomistic infinitesimal strain) that is measured at $\mathbf{x}$ point for the effective strain tensors

of the simulation box $\bar{\boldsymbol{\epsilon}} = \bar{\boldsymbol{\epsilon}}^{(k)}$. $\boldsymbol{\tau}_w(\mathbf{x})$ is the internal Cauchy's stress tensor at $\mathbf{x}$ point that is computed on reference configuration ($\bar{\boldsymbol{\epsilon}} = \mathbf{0}$). Note that $\boldsymbol{\epsilon}_w^{(k)}(\mathbf{x})$ is null by definition for all $\mathbf{x}$ on the reference configuration.

3.2.3. Application of sandwich structure of graphene polymer nanocomposite

The origin of absolute referential, $\mathcal{R}_{Euler}(\mathrm{O}, \mathbf{e}_1, \mathbf{e}_2, \mathbf{e}_3)$, in the Eulerian specification is the center of the graphene sheet and its orientation is defined such that $\mathbf{e}_3$ is normal to the graphene and the triangles in the graphene hexagonal lattice pointing along the $\mathbf{e}_1$ direction (see Figure 2).

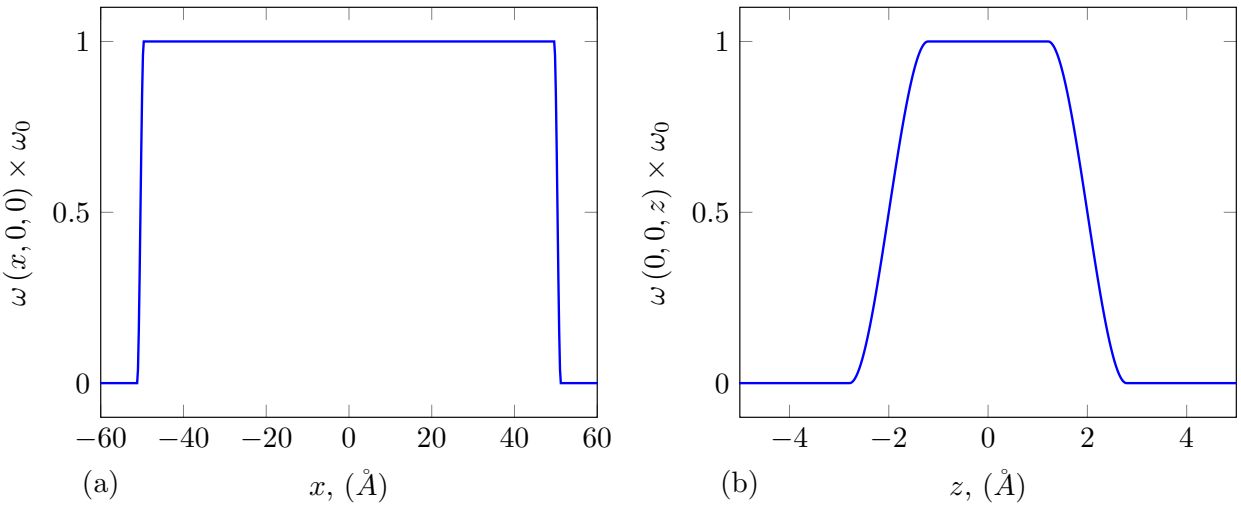

Figure 3: Profiles for weighting function a) along $\mathbf{e}_1$ and b) along $\mathbf{e}_3$.

Here, we want to probe the mechanical properties as a function of the z distance from the graphene sheet. For that reason an anisotropic measuring device with rectangular cuboid shape is used such with lengths $l_1^w = L_x$, $l_2^w = L_y$ and $l_3^w = 4\mathring{A}$. The length l_3^w is chosen to be greater than the C-C bond and small enough to avoid considering graphene atoms when we estimate the interphase properties. We assume that the measure is uniform for all points in the cuboid and that the atoms occupy a small sphere of radius $r^w = 0.77\mathring{A}$ to regularize the weighting function $w(\mathbf{x})$. The atomic radius r^w is chosen as half of the C-C bond of the DREIDING potential [92]. Under these assumptions, the weighting function is defined by a convolution product

$$w\left(\mathbf{x}\right) = \frac{1}{w_0} \int_{\Omega} f^{(Cub)}(\mathbf{x}) f^{(Sph)}(\mathbf{x} - \mathbf{x}') d\mathbf{x}', \tag{34}$$

where w_0 is the normalization constant given by equation (19) and $f^{(Cub)}$ and $f^{(Sph)}$ are the characteristic function of the cuboid and sphere respectively given by

$$f^{(Sph)}\left(\mathbf{x}\right) = 1 - H\left(|\mathbf{x}| - r^w\right), \tag{35}$$

$$f^{(Cub)}\left(\mathbf{x}\right) = \prod_{i=1}^{3} \left(1 - H\left(\left|\mathbf{x}.\mathbf{e}_i - \frac{l_i^w}{2}\right|\right), \right) \tag{36}$$

where $H\left(x\right)$ denotes the Heaviside step function. The representation of weighting function along $\mathbf{e}_1$ and $\mathbf{e}_3$ is shown in Figure 3.

Elongations and simple shears are prescribed to the molecular box to identify the atomistic elastic tensor $\mathbb{C}_w(\mathbf{x})$ at each point. The choice of an anisotropic weight function imposes that the stress field and strain field for these deformations of molecular box depend only on the coordinate z along $\mathbf{e}_3$ axis. Moreover, the components of local infinitesimal strain into the plane $(\mathbf{e}_1, \mathbf{e}_2)$, are equal to the corresponding components

of the effective infinitesimal strain tensor

$$(\boldsymbol{\epsilon}_w)_{11}(\mathbf{x}) = \bar{\boldsymbol{\epsilon}}_{11},\ (\boldsymbol{\epsilon}_w)_{22}(\mathbf{x}) = \bar{\boldsymbol{\epsilon}}_{22},\ (\boldsymbol{\epsilon}_w)_{12}(\mathbf{x}) = \bar{\boldsymbol{\epsilon}}_{12} \qquad \forall \mathbf{x}. \tag{37}$$

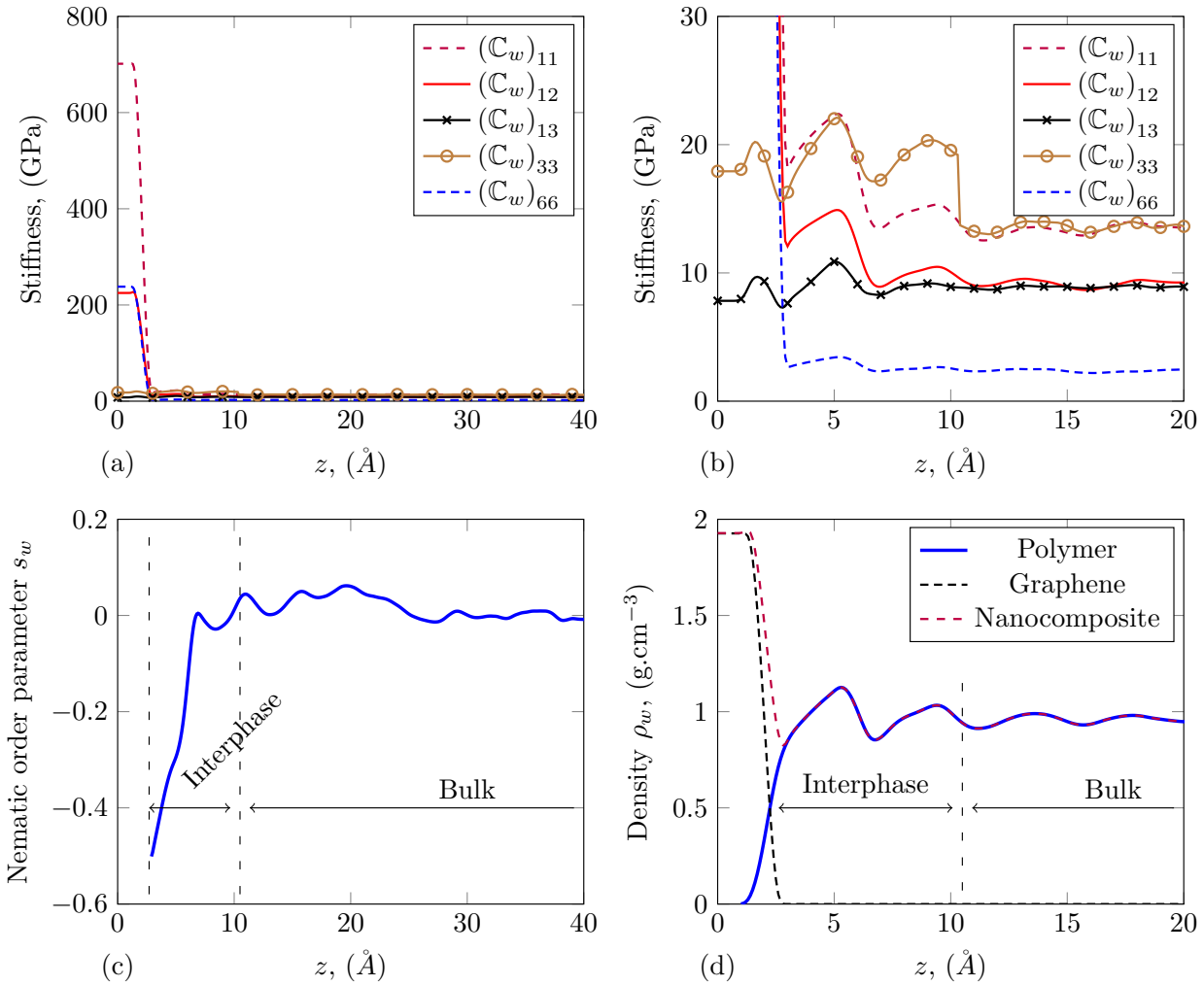

Figure 4: (a) and (b) Evolution of stiffness tensor components with Voigt notation as a function of the normal distance, z, from the graphene layer; (c) Nematic order parameter, s_w vs z; (d) Evolution of density ρ_w of polymer, graphenes and nano composite as a function of the normal distance, z.

This post-processing has shown that the stiffness tensor components with Voigt notation verify that $\forall \mathbf{x}$, $(\mathbb{C}_w)_{11}(\mathbf{x}) \approx (\mathbb{C}_w)_{22}(\mathbf{x})$, $(\mathbb{C}_w)_{31}(\mathbf{x}) \approx (\mathbb{C}_w)_{32}(\mathbf{x})$ and $\forall I \geq 4$, $(\mathbb{C}_w)_{I1}(\mathbf{x}) \approx (\mathbb{C}_w)_{I2}(\mathbf{x}) \approx 0$; and $\forall I < 6$, $(\mathbb{C}_w)_{I6}(\mathbf{x}) \approx 0$. The Figure 4a,b show the evolution of $(\mathbb{C}_w)_{11}$, $(\mathbb{C}_w)_{12}$, $(\mathbb{C}_w)_{13}$, $(\mathbb{C}_w)_{33}$ and $(\mathbb{C}_w)_{66}$ with the distance to the graphene z. Substantial increase of one order of magnitude of the stiffness components in graphene plane ($(\mathbb{C}_w)_{11}$, $(\mathbb{C}_w)_{12}$ and $(\mathbb{C}_w)_{66}$) is shown for $z < 2.5$Å due to graphene sheet (see Figure 4a). In the interphase area, $2.5\text{Å} \leq z \leq 10.5\text{Å}$, the stiffness components $(\mathbb{C}_w)_{11}$, $(\mathbb{C}_w)_{12}$ and $(\mathbb{C}_w)_{33}$ are 40% higher than in the bulk part $z \geq 10.5$Å (see Figure 4b), while $(\mathbb{C}_w)_{13}$ and $(\mathbb{C}_w)_{66}$ seem to be the same as the polymer bulk. Thus, the thickness of the interphase region is identified as 10.5 Å.

Due to the slip at the polymer/graphene interface (see Figure 5b), the local strain, $\boldsymbol{\epsilon}_w(\mathbf{x})$ and the local stress increment, $\boldsymbol{\sigma}_w(\mathbf{x})$, in the polymer remains zero for all shears in the graphene plane. It is therefore impossible to identify with this method the stiffness tensor components $(\mathbb{C}_w)_{I4}$ and $(\mathbb{C}_w)_{I5}$. For convenient

reasons, we assume that $(\mathbb{C}_w)_{44}(\mathbf{x}) = (\mathbb{C}_w)_{55}(\mathbf{x}) = (\mathbb{C}_w)_{66}(\mathbf{x})$ and $\mathbb{C}_{I4}(\mathbf{x}) = \mathbb{C}_{I5}(\mathbf{x}) = 0$ for all $\mathbf{x}$ in the polymer region.

The stiffness increase in the interphase region appears to be related to the increase in atomic density, $\rho_w(\mathbf{x})$ which results in an increase in the van der Waals interaction density. Figure 4d shows the local density of graphene, polymer and composite systems as a function of the z distance from the graphene sheet. The density of the graphene polymer composite with sandwich structure is dominated by the density of graphene in the midplane and by the density of polymer for the rest part. We can see a dense packing of polymer mass close to graphene layer called interphase zone, which is due to the adsorption of the chains on faces of graphene sheets. In addition to the density effect, the stiffness increase in the interphase along the graphene sheet plan ($(\mathbb{C}_w)_{11}$, $(\mathbb{C}_w)_{22}$ and $(\mathbb{C}_w)_{12}$) is also due to the orientation of the covalent bonds inside of polymer macromolecules into the plane $(\mathbf{e}_1, \mathbf{e}_2)$. This local conformation change is evidenced by the nematic order parameter s_w (see Figure 4c), which is defined by

$$s_w(\mathbf{x}) = \frac{1}{\rho_b(\mathbf{x})} \sum_{\mathcal{B}^{(p)}} \left(\frac{3\left(\mathbf{n}_{\alpha\beta}.\mathbf{e}_3\right)^2 - 1}{2} \right) b_w\left(\mathbf{x}; \mathbf{r}_\alpha(t), \mathbf{r}_\beta(t)\right) \tag{38}$$

where $\mathcal{B}^{(p)}$ is the set of covalent bonds in the polymer; $\mathbf{e}_3$ is the unit normal of graphene; $\mathbf{n}_{\alpha\beta} = (\mathbf{r}_\alpha - \mathbf{r}_\beta)/r_{\alpha\beta}$ is the unit vector which defined the covalent bond direction between two CH_2 atom group α and β along the polymer chain; $b_w(\mathbf{x}; \mathbf{r}_\alpha(t), \mathbf{r}_\beta(t))$ is the bond function defined Eq. (27) and $\rho_b(\mathbf{x}) = \sum_{\mathcal{B}^{(p)}} b_w(\mathbf{x}; \mathbf{r}_\alpha(t), \mathbf{r}_\beta(t))$ is a normalization constant which corresponds to the local bond density at $\mathbf{x}$. We can see on the Figure 4c a decrease of the nematic order parameter s_w in the interphase. Generally, the nematic order s_w is used to describe the orientational order of a nematic liquid crystal. For a completely random and isotropic sample, $s_w = 0$, whereas for a perfectly aligned sample along $\mathbf{e}_3$ axis, $s = 1$. In addition, $s = -1/2$ denotes that all the bonds are in the plan perpendicular to $\mathbf{e}_3$. Therefore, it indicates that in the interfacial zone close to the graphene sheets, the polymer chains turn to be paralleled to the graphene layer.

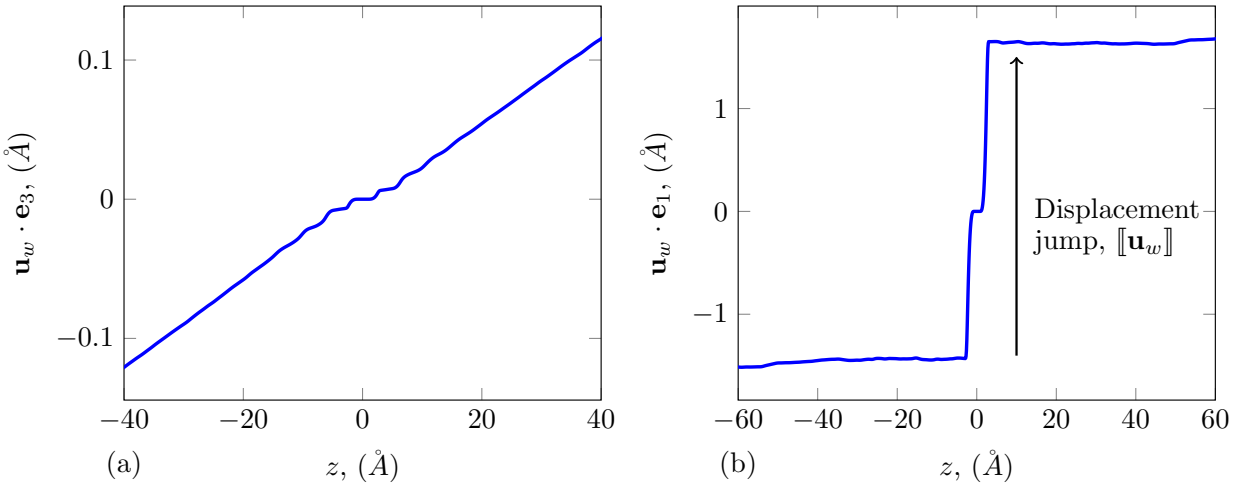

Figure 5: Evolution of displacement components as a function of the normal distance, z, from the graphene layer. (a) $\mathbf{u}_w \cdot \mathbf{e}_3$ for a elongation of $\epsilon_n = 0.3\%$ normal to the graphene sheet, $\bar{\boldsymbol{\epsilon}} = \epsilon_n \mathbf{e}_3 \otimes \mathbf{e}_3$. (b) $\mathbf{u}_w \cdot \mathbf{e}_1$ for a simple shear of $\gamma = 3\%$ in a direction $\mathbf{e}_1$ on a graphene plane, $\bar{\boldsymbol{\epsilon}} = \frac{\gamma}{2}(\mathbf{e}_3 \otimes \mathbf{e}_1 + \mathbf{e}_1 \otimes \mathbf{e}_3)$.

Moreover, the ALIAS method makes it possible to define a displacement field $\mathbf{u}_w$. Figure 5 represents the components of displacement fields, $\mathbf{u}_w$ along the normal of graphene sheet for an elongation of $\epsilon_n = 0.3\%$ normal to the graphene sheet, $\bar{\boldsymbol{\epsilon}} = \epsilon_n \mathbf{e}_3 \otimes \mathbf{e}_3$ (see Figure 5a) and for an simple shear of $\gamma = 3\%$ in a direction $\mathbf{e}_1$ on a graphene plane, $\bar{\boldsymbol{\epsilon}} = \frac{\gamma}{2}(\mathbf{e}_3 \otimes \mathbf{e}_1 + \mathbf{e}_1 \otimes \mathbf{e}_3)$ (see Figure 5b).

As shown in Figure 5a, the component $\mathbf{u}_w \cdot \mathbf{e}_3$ of displacement field evolves linear in polymer bulk

($z < 10.5$ and $z > 10.5$), which means that the strain is homogeneous there ($\approx 0.32\%$). In the central part corresponding to the interphase, discontinuities are observed. Note that the average slope is lower there ($\approx 0.23\%$), which is in agreement with the fact that the interphase is stiffer.

Figure 5b shows sharp discontinuities of the displacement fields component $\mathbf{u}_w \cdot \mathbf{e}_1$ on both sides of graphene sheet. Moreover, the displacement field remains constant in the polymer region. These two facts indicate that the deformation applied to the atomic box is accommodated by slips at the interfaces between graphene and polymer.

3.3. Identification of imperfect interface elastic parameters

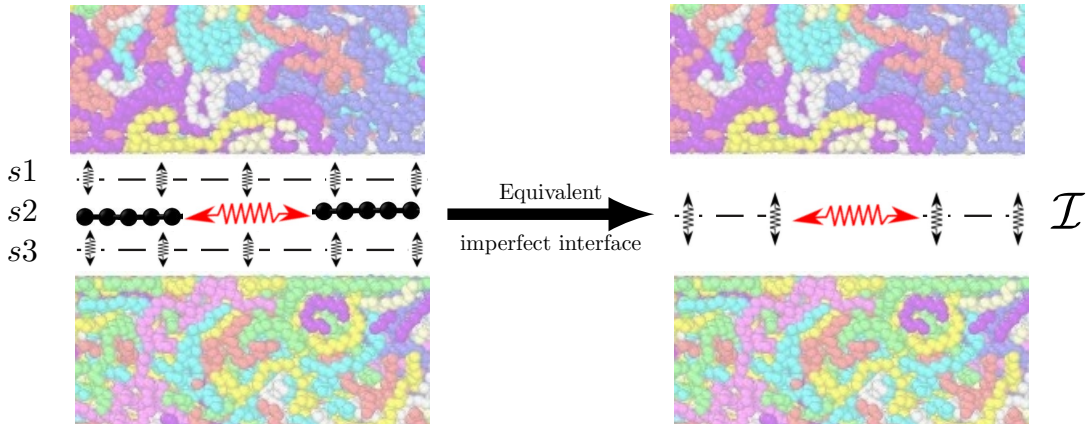

Figure 6: Scheme of the three layers of the imperfect interface $\mathcal{I}$.

For the identification of interface parameters, we write the surface free energy ϕ^s as the sum of three contributions as shown in Figure 6: one for the graphene and two for the interfaces polymer/graphene. Therefore, the three layers description of the imperfect interface is used. We assume that the elastic parameters of the imperfect interface are constant along the graphene sheet for the sake of simplicity and consistency with the previous section.

Following the classification in [45], the graphene layer can be considered as an elastic interface, denoted by $s2$, *i.e.* it is kinematically coherent ($[\![\mathbf{u}]\!]|_{s2} = \mathbf{0}$) but kinetically non-coherent ($[\![\mathbf{t}]\!]|_{s2} \neq \mathbf{0}$). The free energy of $s2$ is defined by

$$\phi^{s2} = \frac{1}{2}\boldsymbol{\epsilon}^{s2} : \mathbb{C}^{s2} : \boldsymbol{\epsilon}^{s2} + \boldsymbol{\tau}^{s2} : \boldsymbol{\epsilon}^{s2} + \phi_0^{s2}, \tag{39}$$

where $\mathbb{C}^{s2}$ is the fourth order surface stiffness tensor of graphene, $\boldsymbol{\tau}^{s2}$ is the internal surface stress and $\boldsymbol{\epsilon}^{s2}$ is the surface strain tensor into the graphane sheet.

The graphene/polymer interfacial regions can be assumed as cohesive interfaces, denoted $s1$ and $s3$, *i.e.* it is kinematically non-coherent ($[\![\mathbf{u}]\!]|_{s1} \neq \mathbf{0}$ and $[\![\mathbf{u}]\!]|_{s3} \neq \mathbf{0}$) but kinetically coherent ($[\![\mathbf{t}]\!]|_{s1} = [\![\mathbf{t}]\!]|_{s3} = \mathbf{0}$). The cohesive laws for interface $s1$ and $s3$ is

$$\boldsymbol{\sigma}|_{s1}.\mathbf{e}_3 = \mathbf{K}^{s1}[\![\mathbf{u}]\!]|_{s1}, \quad \boldsymbol{\sigma}|_{s3}.\mathbf{e}_3 = \mathbf{K}^{s3}[\![\mathbf{u}]\!]|_{s3}, \tag{40}$$

where $\mathbf{K}^{s1}$ and $\mathbf{K}^{s3}$ are the second order cohesive stiffness matrix of the interface $s1$ and $s3$. The free energy of $s1$ and $s3$ are defined by

$$\phi^{s1} = \frac{1}{2}[\![\mathbf{u}]\!]|_{s1}.\mathbf{K}^{s1}.[\![\mathbf{u}]\!]|_{s1} + \phi_0^{s1}, \quad \phi^{s3} = \frac{1}{2}[\![\mathbf{u}]\!]|_{s3}.\mathbf{K}^{s3}.[\![\mathbf{u}]\!]|_{s3} + \phi_0^{s3}, \tag{41}$$

where $\phi_0^s = \phi_0^{s1} + \phi_0^{s2} + \phi_0^{s3}$.

The kinematic compatibility across the graphene sheet $s2$ enforces that the jump of displacement field in the equivalent imperfect interface is

$$[\![\mathbf{u}]\!] = \mathbf{u}|_{s3}^{+} - \mathbf{u}|_{s1}^{-} = \left(\mathbf{u}|_{s3}^{+} - \mathbf{u}^{g}\right) + \left(\mathbf{u}^{g} - \mathbf{u}|_{s1}^{-}\right) = [\![\mathbf{u}]\!]|_{s1} + [\![\mathbf{u}]\!]|_{s3}. \tag{42}$$

In equation (42), "+" and "-" correspond to the upper and lower surface of the interface with respect to the normal direction $\mathbf{e}_3$. The results of atomistic simulations suggest that the displacement jumps across interface $s1$ and $s3$ are equal. For the sake of simplicity, we assume that $[\![\mathbf{u}]\!]|_{s1} = [\![\mathbf{u}]\!]|_{s3} = [\![\mathbf{u}]\!]/2$, which implies that the displacement field, $\mathbf{u}^g$ ($\mathbf{u}^g = \mathbf{u}|_{s2}^{+} = \mathbf{u}|_{s2}^{-} = \mathbf{u}|_{s1}^{+} = \mathbf{u}|_{s3}^{-}$), and the strain fields, $\boldsymbol{\epsilon}^{s2}$, on the graphene sheet are given by

$$\mathbf{u}^g = \frac{\mathbf{u}|_{s3}^{+} + \mathbf{u}|_{s1}^{-}}{2}, \qquad \boldsymbol{\epsilon}^{s2}(\mathbf{x}) = \frac{1}{2}\left(\nabla^s \mathbf{u}^g(\mathbf{x}) + (\nabla^s \mathbf{u}^g)^T(\mathbf{x})\right). \tag{43}$$

Keeping in mind the cohesive law for the equivalent imperfect interface as

$$\mathbf{K}^s [\![\mathbf{u}]\!] = \mathbf{t}^s = \frac{(\boldsymbol{\sigma}|_{s1} + \boldsymbol{\sigma}|_{s3}).\mathbf{e}_3}{2}, \tag{44}$$

introducing the cohesive laws of the interface $s1$ and $s3$, and using the equality of jump displacement across $s1$ and $s3$, we obtain

$$\mathbf{K}^s = \frac{1}{4}\left(\mathbf{K}^{s1} + \mathbf{K}^{s3}\right) = \frac{1}{2}\mathbf{K}^{s1} = \frac{1}{2}\mathbf{K}^{s3}. \tag{45}$$

The two last equalities come from the mirror symmetry of the system with respect to the graphene plane which implies that $\mathbf{K}^{s1} = \mathbf{K}^{s3}$.

The additivity of specific free energy and the equation (45) gives

$$\phi^s = \phi^{s1} + \phi^{s2} + \phi^{s3}, \tag{46}$$

$$\phi^s = [\![\mathbf{u}]\!]|_{s1}.\mathbf{K}^s.[\![\mathbf{u}]\!]|_{s1} + \frac{1}{2}\boldsymbol{\epsilon}^s : \mathbb{C}^{s2} : \boldsymbol{\epsilon}^s + [\![\mathbf{u}]\!]|_{s3}\mathbf{K}^s.[\![\mathbf{u}]\!]|_{s3} + \phi_0^s. \tag{47}$$

After establishing the new expression of specific free energy of the imperfect interface ϕ^s, the identification of stiffness tensor $\mathbf{K}^s$ is detailed. At atomic scale we impose elementary rigid body translation of graphene sheet, $\mathbf{d} = d_1\mathbf{e}_1 + d_2\mathbf{e}_2 + d_3\mathbf{e}_3$ (see e.g. Fig. 7a for translation along $\mathbf{e}_1$). The polymer atoms displacements are kept fixed so that the variation of potential energy is only due to the displacement discontinuity at the interface and $[\![\mathbf{u}]\!]|_{s1} = -[\![\mathbf{u}]\!]|_{s3} = \mathbf{d}$. Assuming that the temperature is 0 K in our simulations, the variation of free energy for a translation $\mathbf{d}$ of graphene is given by the variation of potential energy

$$\Delta\mathcal{U} = \left\langle \phi - \phi^{(0)} \right\rangle = \int_\Omega \phi - \phi_0 \,\mathrm{d}\Omega + \int_{\mathcal{I}} \phi^s - \phi_0^s \,\mathrm{d}S \tag{48}$$

$$= S\left([\![\mathbf{u}]\!]|_{s1}.\mathbf{K}^s.[\![\mathbf{u}]\!]|_{s1} + [\![\mathbf{u}]\!]|_{s3}\mathbf{K}^s.[\![\mathbf{u}]\!]|_{s3}\right) \tag{49}$$

$$= 2S\left(\mathbf{d} \cdot \mathbf{K}^s \cdot \mathbf{d}\right) \tag{50}$$

where S is the graphene sheet surface. The last equation shows that the potential energy is a quadratic function of $\mathbf{d}$ defined by the six independant components of the symetric second order stiffness tensor $\mathbf{K}^s$. For the identification, we compute a set of 37 values of the variation of potential energy $\Delta\mathcal{U}$ to estimate the stiffness tensor $\mathbf{K}^s$ by the least squares method (see supplementary information for details). We assume that the stiffness tensor $\mathbf{K}^s$ is diagonal $(\mathbf{K}^s)_{23} = (\mathbf{K}^s)_{31} = (\mathbf{K}^s)_{12} = 0$ MPa.nm^{-1}, for the sake of simplicity. The cohesive part of the general imperfect interface is very anistropic because the stiffness associated to the opening mode perpendicular to the graphene $(\mathbf{K}^s)_{33} = 52960$ MPa.nm^{-1} is five order of magnitude than the stiffness associated to the slips along graphene plane $(\mathbf{K}^s)_{11} = (\mathbf{K}^s)_{22} = 8.50$ MPa.nm^{-1}.

This identification method allows to identify the Critical Resolved Shear Stress (CRSS) associated to the slip in the graphene plane by computation of the local shear stress. Fig. 7b shows the evolution of the

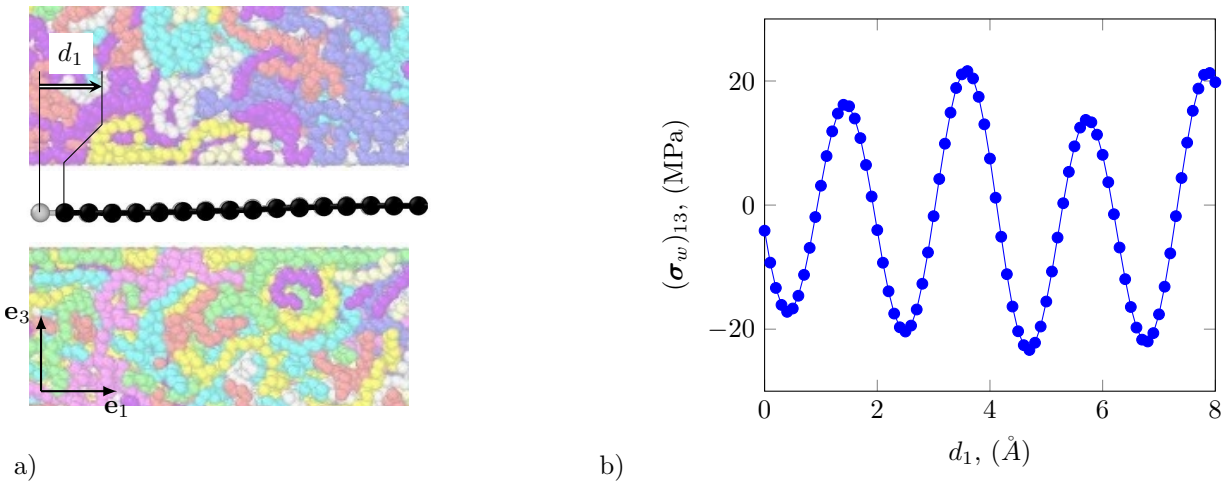

Figure 7: a) Scheme of graphene sheet translation along $\mathbf{e}_1$. b) Evolution of shear stress in a graphene plane for a translation along $\mathbf{e}_1$.

local shear stress $(\boldsymbol{\sigma}_w)_{13}$ as function of d for a translation of graphene sheet along $\mathbf{e}_1$. The curve has the same periodicity as that of the graphene lattice. There are two maxima in one period. The smaller one provides the value of CRRS, $\tau^\star \approx 17$ MPa. Note that this value remains approximatively the same for all slip directions into the graphene plane.

The surface elasticity tensor is identified by the method used for the bulk. Indeed, the fourth-order stiffness tensor $\mathbb{C}_w$ is identified on the graphene sheet ($z = 0$). Then, $\mathbb{C}^s$, is deduced from (see *e.g.* [98]).

$$\mathbb{C}^s = h\left(\mathbb{C}_w - \frac{(\mathbb{C}_w : \mathbf{N}) \otimes (\mathbb{C}_w : \mathbf{N})}{\mathbf{N} : \mathbb{C}_w : \mathbf{N}}\right), \tag{51}$$

where $\mathbf{N} = \mathbf{e}_3 \otimes \mathbf{e}_3$ and $h = 4\mathring{A}$ is the graphene sheet thickness. The h value is chosen as the full width at half maximum of the curve of graphene density ρ_w *vs.* z (see Figure 4d). In this work, $\mathbb{C}^s$ is given $\mathbb{C}^s_{11} = \mathbb{C}^s_{22} = 280$ GPa.nm, $\mathbb{C}^s_{12} = 90$ GPa.nm, $\mathbb{C}^s_{66} = 95$ GPa.nm and $\mathbb{C}^s_{ij} = 0$ GPa.nm for other components.

4. Discussion

4.1. Summary of the identification of elastic parameters

The results of the previous section suggest that polymer/graphene nanocomposite can be modeled by a five layer composite: an imperfect interface for graphene ($\mathcal{I}$), two interphase layers (Ω^2 and Ω^3) with a thickness, $t_I = 10.5$ Å and two layers for polymer bulk (Ω^1 and Ω^4) see Figure 8b. The mean values of the elastic constants in Voigt notation for each layer are given in Table 2.

The elastic behavior of the polymer bulk is isotropic and can be defined by the Lame's coefficients $\lambda^b = 9.0$ GPa and $\mu^b = 2.3$ GPa, such as $\mathbb{C}^b_{11} = \mathbb{C}^b_{22} = \mathbb{C}^b_{33} = \lambda^b + 2\mu^b$; $\mathbb{C}^b_{12} = \mathbb{C}^b_{23} = \mathbb{C}^b_{31} = \lambda^b$ and $\mathbb{C}^b_{44} = \mathbb{C}^b_{55} = \mathbb{C}^b_{66} = \mu^b$. The elastic behavior of the polymer interphase is transverse isotropic, it can be defined by five coefficients, such as $\mathbb{C}^I_{11} = \mathbb{C}^I_{22} = 17$ GPa; $\mathbb{C}^I_{12} = 11.4$ GPa, $\mathbb{C}^b_{23} = \mathbb{C}^b_{31} = 9.1$ GPa; $\mathbb{C}^I_{44} = \mathbb{C}^I_{55} = 2.3$ GPa and $\mathbb{C}^I_{66} = (\mathbb{C}^I_{11} - \mathbb{C}^I_{12})/2$. The surface elasticity of imperfect interface is isotropic, it is defined by surfacic Lame's coefficients $\lambda^b = 95$ GPa.nm and $\mu^b = 90$ GPa.nm, such as $\mathbb{C}^s_{11} = \mathbb{C}^s_{22} = \lambda^s + 2\mu^s$; $\mathbb{C}^b_{12} = \lambda^s$ and $\mathbb{C}^b_{66} = \mu^s$. The cohesive stiffness of imperfect interface is isotropic into the graphene plane ($\mathbf{K}^s_{11} = \mathbf{K}^s_{22}$ and $\mathbf{K}^s_{12} = \mathbf{K}^s_{23} = \mathbf{K}^s_{31} = 0$ MPa.nm^{-1}), with a huge mechanical contrast between the out of graphene plane stiffness and the in plane stiffness ($\mathbf{K}^s_{33}/\mathbf{K}^s_{11} \approx 10^5$).

It is important to note that the results depend on the weight function, $w(\mathbf{x})$ and therefore on the shape and size of our measuring tools. Nevertheless, the mean strain computed with the atomistic displacement,

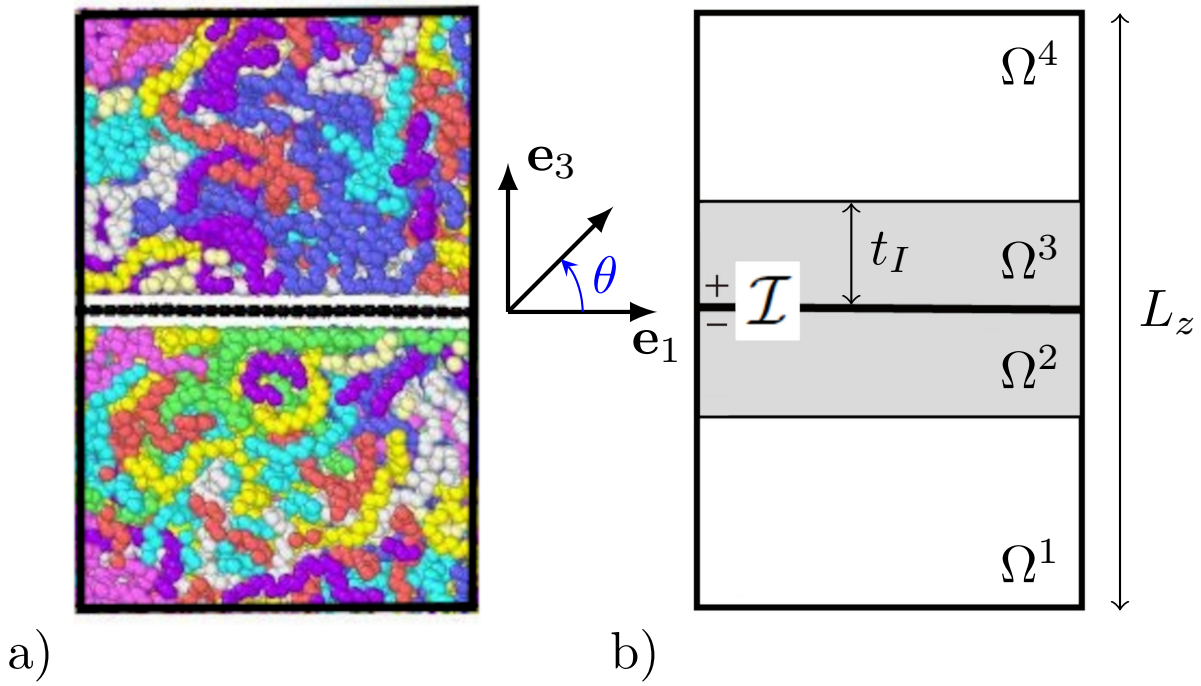

Figure 8: a) Atomistic configuration; b) Equivalent continuum model with imperfect interface and interphases.

$\mathbf{u}_w(\mathbf{x})$ is equal to the the effective strain of the atomistic simulation box $\overline{\boldsymbol{\epsilon}}$, and that the effective properties are the same for the atomic and continuum models (cf. following section and Table 2). Another area for improvement is taking the temperature into account. Indeed, all the results are obtained at zero temperature which explains why the Young's modulus of polymer bulk, $E_b \approx 6.4$ GPa, has the same order of magnitude as that of an amorphous polymer below its secondary transition temperature [99]. We estimate that the ratio between Young's modulus of interphase, E_I and bulk remains qualitatively the same $E_I/E_b \approx 1.5$ for temperatures below the glass transition temperature of the bulk and for much higher temperatures. We issue a large reserve for a temperature range around the glass transition temperature of the bulk because it is possible that the glass transition temperature of the interphase is different [100, 101], which would generate a change of one or two orders of magnitude of the ratio E_I/E_b.

4.2. Effective properties of sandwich structure

We use the framework derived by Chatzigeorgiou et al [45] to define the macro strain tensor $\overline{\boldsymbol{\epsilon}}$ (or the mean strain tensor of the sandwich RVE of the Fig. 8 a):

$$\overline{\boldsymbol{\epsilon}} = \frac{1}{|\Omega|}\int_\Omega \boldsymbol{\epsilon}\,\mathrm{d}V + \frac{1}{|\Omega|}\int_{\mathcal{I}} \frac{1}{2}\left(\mathbf{n}_{\mathcal{I}} \otimes [\![\mathbf{u}]\!] + [\![\mathbf{u}]\!] \otimes \mathbf{n}_{\mathcal{I}}\right)\mathrm{d}S, \tag{52}$$

where $\mathbf{n}_{\mathcal{I}}$ is the unit normal vector to the imperfect interface at a given point. The macro stress $\overline{\boldsymbol{\sigma}}$ (or the mean stress tensor of the sandwich RVE) is defined by

$$\overline{\boldsymbol{\sigma}} = \frac{1}{|\Omega|}\int_\Omega \boldsymbol{\sigma}\,\mathrm{d}V + \frac{1}{|\Omega|}\int_{\mathcal{I}} \boldsymbol{\sigma}^s\,\mathrm{d}S \tag{53}$$

The effective stiffness tensor $\overline{\mathbb{C}}_C$ of the equivalent continuum model, which linearly connects the macro stress and strain ($\overline{\boldsymbol{\sigma}} = \overline{\mathbb{C}}_C : \overline{\boldsymbol{\epsilon}}$), is computed by numerical homogenization with periodic boundary condi-

Table 2: Identified elastic constants of the continuum model in Voigt notation.

Polymer bulk

$$\mathbb{C}^b = \begin{bmatrix} 13.6 & 9.0 & 9.0 & 0 & 0 & 0 \\ 9.0 & 13.6 & 9.0 & 0 & 0 & 0 \\ 9.0 & 9.0 & 13.6 & 0 & 0 & 0 \\ 0 & 0 & 0 & 2.3 & 0 & 0 \\ 0 & 0 & 0 & 0 & 2.3 & 0 \\ 0 & 0 & 0 & 0 & 0 & 2.3 \end{bmatrix} \text{ GPa}$$

Polymer interphase

$$\mathbb{C}^I = \begin{bmatrix} 17.0 & 11.4 & 9.1 & 0 & 0 & 0 \\ 11.4 & 17.0 & 9.1 & 0 & 0 & 0 \\ 9.1 & 9.1 & 19.2 & 0 & 0 & 0 \\ 0 & 0 & 0 & 2.3 & 0 & 0 \\ 0 & 0 & 0 & 0 & 2.3 & 0 \\ 0 & 0 & 0 & 0 & 0 & 2.9 \end{bmatrix} \text{ GPa}$$

Imperfect Interface

$$\mathbb{C}^s = \begin{bmatrix} 280 & 90 & 0 & 0 & 0 & 0 \\ 90 & 280 & 0 & 0 & 0 & 0 \\ 0 & 0 & 0 & 0 & 0 & 0 \\ 0 & 0 & 0 & 0 & 0 & 0 \\ 0 & 0 & 0 & 0 & 0 & 0 \\ 0 & 0 & 0 & 0 & 0 & 95 \end{bmatrix} \text{ GPa.nm}$$

$$\mathbf{K}^s = \begin{bmatrix} 8.5 & 0 & 0 \\ 0 & 8.5 & 0 \\ 0 & 0 & 52960 \end{bmatrix} \text{ MPa.nm}^{-1}$$

Effective stiffness of RVE ($L_z = 10$ nm)

Continuum model

$$\overline{\mathbb{C}}_C = \begin{bmatrix} 43.3 & 18.7 & 8.77 & 0 & 0 & 0 \\ 18.7 & 43.3 & 8.77 & 0 & 0 & 0 \\ 8.77 & 8.77 & 14.1 & 0 & 0 & 0 \\ 0 & 0 & 0 & 0.079 & 0 & 0 \\ 0 & 0 & 0 & 0 & 0.079 & 0 \\ 0 & 0 & 0 & 0 & 0 & 12.3 \end{bmatrix} \text{ GPa}$$

Atomistic model

$$\overline{\mathbb{C}}_A = \begin{bmatrix} 43.3 & 18.7 & 8.8 & 0.0 & 0.0 & 0.0 \\ 18.7 & 43.3 & 8.8 & 0.0 & 0.0 & 0.0 \\ 8.8 & 8.8 & 14.1 & 0.0 & 0.0 & 0.0 \\ 0.0 & 0.0 & 0.0 & 0.0 & 0.0 & 0.0 \\ 0.0 & 0.0 & 0.0 & 0.0 & 0.0 & 0.0 \\ 0.0 & 0.0 & 0.0 & 0.0 & 0.0 & 12.3 \end{bmatrix} \pm 0.1 \text{ GPa}$$

tions satisfying the extended Hill-Mandel condition [45] (see Supplementary Information for details). We use the finite element method to discretize the solution space with linear tetrahedrons for bulk part and linear triangles for interfaces. The effective behavior of the sandwich structure, presented in Table 2, is transversally isotropic because the microstructure and the elastic properties of phases are isotropic along the graphene plane. In addition, the effective stiffness depends on the RVE size L_z. It is possible to obtain an analytic expression of the effective stiffness coefficient $(\overline{\mathbb{C}}_C)_{ij}$ in the case of RVE with a sandwich structure. The theoretical study of this size effect will be the subject of a future work, but here we preferred to study the influence of the interface and the interphase on the RVE anisotropy.

To validate the ALIAS methodolgy, we estimate directly by atomic simulations the effective stiffness tensor, $\overline{\mathbb{C}}_A$, following the procedure introduced for polymer based materials by Theodorou and Suter [102] (see Supplementary Information for details). We believe that our approach is validated because we find the same effective module $\overline{\mathbb{C}}_C = \overline{\mathbb{C}}_A$, with the exception of the components $(\overline{\mathbb{C}}_A)_{44}$ and $(\overline{\mathbb{C}}_A)_{55}$ which cannot be obtained by atomistic simulations because of the sliding at the polymer/graphene interface (cf. the end of section 3.2.3).

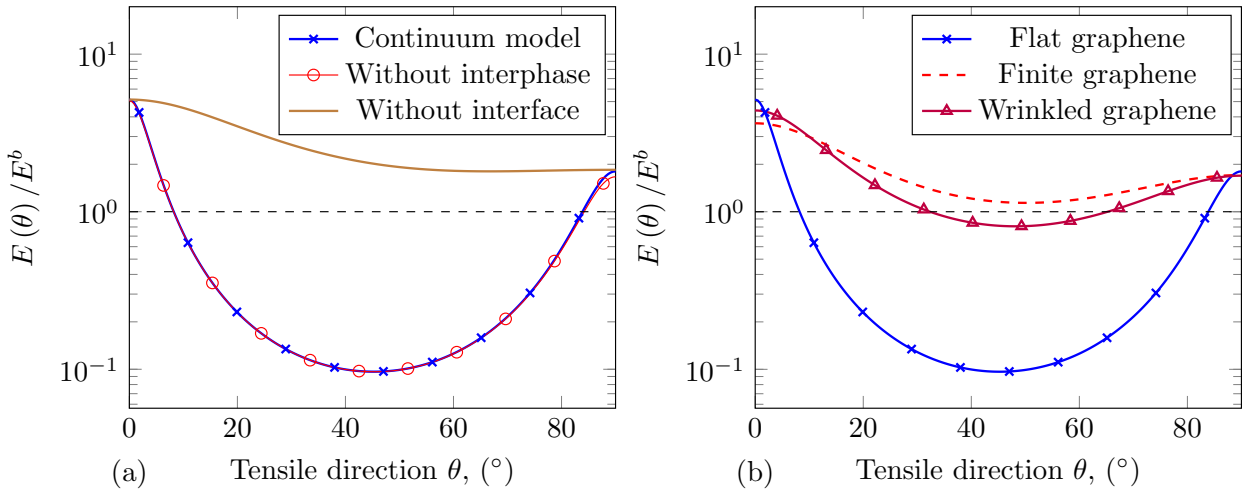

Figure 9: Young's modulus normalized by that of the bulk polymer E_b as function of the angle, θ, between the tensile direction and the vector $\mathbf{e}_1$ into the plane $(\mathbf{e}_1, \mathbf{e}_3)$ (see Supplementary Information for compuation details of $E(\theta)$). a) Comparison between the full continuum model (with interface and interphase) and a model without interphase and another one without the cohesive part of imperfect interface ($[\![\mathbf{u}]\!] = \mathbf{0}$) b) Illustration of the effect finite size of graphene and wrinkle of graphene on the stiffness anisotropy.

To show this anisotropy, we plot in Figure 9a the Young's modulus $E(\theta)$ normalized by Young's modulus of polymer E_b as function of the θ angle (see Figure 8) between the tensile direction and the vector $\mathbf{e}_1$ into the plane $(\mathbf{e}_1, \mathbf{e}_3)$. We use the effective stiffness tensor $\overline{\mathbb{C}}_C$ to compute $E(\theta)$, the demonstration of the used formula is provided in Supplementary Informaiton. We notice that for tensile directions that are perpendicular to the graphene ($\theta = 90°$) and aligned with graphene ($\theta = 0°$) the Young's modulus is greater than that of the polymeric matrix. It is even five times larger in the graphene plane due to the extraordinary stiffness of graphene. On the other hand, for a wide angular range ($6° \leq \theta \leq 86°$), the Young's modulus is much lower than that of the polymer, going up to more than one order of magnitude for angular range ($22° \leq \theta \leq 68°$). This is due to the superlubricity of graphene (see e.g. [103], for review) which generates very low shear stiffness and CRSS.

To compare the influence of the interphase and the interface on the elastic properties, we plot in Figure 9a the Young's modulus normalized as a function of the θ angle for one model "without interphase" ($\mathbb{C}^b = \mathbb{C}^i$) and another one "without interface", i.e. without displacement discontinuities at graphene interfaces ($[\![\mathbf{u}]\!] = \mathbf{0}, \mathbf{K}^s_{ii} \to \infty$). It is clear that the interphase has no significant effects on the Young modulus because the curves of the models with and without interphase are superposed; with the exception of an increase in

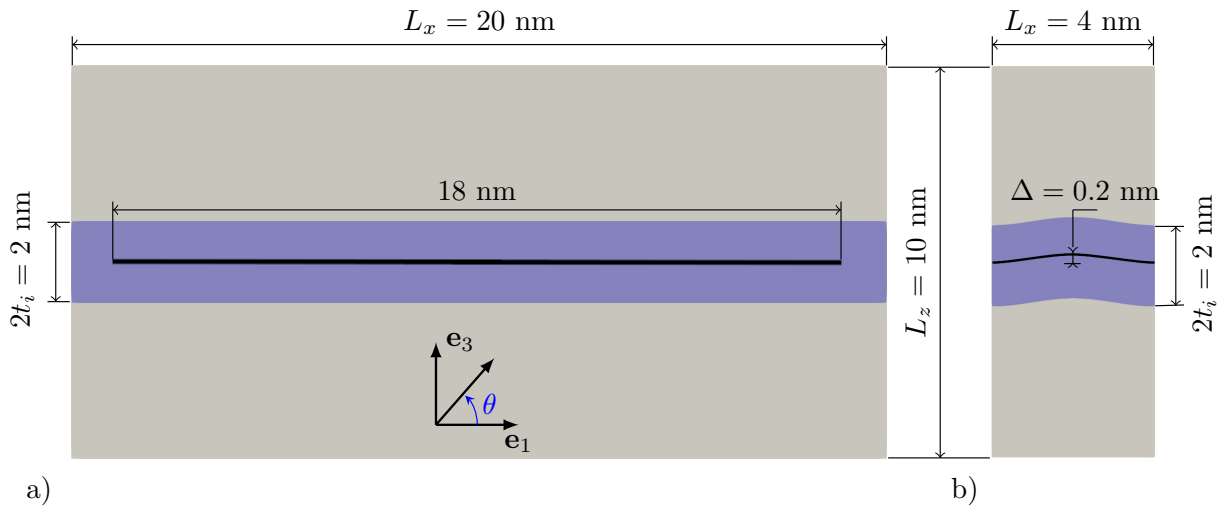

Figure 10: RVE scheme for finite element simulations: a) with finite size graphene; b) with the wrinkled graphene. Note that the 3D RVE model is obtained by an extrusion of these 2D sketches. The associated meshes are given in supplementary information.

Table 3: Influence on the effective properties of graphene modifications

	Stiffness (E)	Yield stress (σ_y)	Toughness (K_{Ic})	Electrical resistivity (ρ_e)
Chemical modified graphene	↗	↗	↘	↗
Geometrical modification (wrinkling, border)	↗	open question	open question	↗

the Young's modulus of 10% for a tensile direction perpendicular to graphene ($\theta = 90°$), which is not visible on the graph. Conversely, the interface acts as a notable softener effect because the model without interface has a Young's modulus always higher than that of the polymer.

We can conclude that one of the ways to increase the Young's modulus of nanocomposite without microstructure change is to increase the interfacial cohesion between the polymer and the graphene by chemical route such as grafting. Nevertheless, this involves a compromise for the material designer between stiffness and electrical conductivity. In fact, the exceptional electrical conductivity of graphene is altered when the perfection of the 2D crystal is broken. The chemical interface modification will also modify the CRSS, which would tend to increase the yield stress and decrease the toughness. Indeed, the toughness material is able to dissipate energy by anelastic mechanisms such as interfacial sliding before propagating a critical crack. Therefore, the CRSS increasing, induced by the chemical grafting of graphene, should decrease the number of active slip sites in a volume element and thus reduce the toughness. We fall back into one of the classic conflicts between strength and toughness [104].

Another way to increase the Young's modulus is to change the geometry of the system by either adding the GNP extremities or introducing a graphene wrinkle. Figure 10 shows model microstructures, one with the GNP extremities and the other with wrinkled graphene. Figure 9b shows the effect of these geometric changes on the Young's modulus anisotropy. Taking into account the GNP extremities increases the Young's modulus by one order of magnitude for angular range $20° \leq \theta \leq 70°$. However the same simulation with "without interface", *i.e.* without displacement discontinuity ($[\![\mathbf{u}]\!] = \mathbf{0}$), shows an increase in Young's modulus going up to double for $\theta = 45°$. The other geometric effect which increases the Young's modulus is the GNP wrinkling. In this case, the effect on Young's modulus is similar to that of taking into account the GNP extremity (see Figure 9b) with higher moduli in directions ($\theta = 0°$ and $90°$). Note that the curvature

effects is taken into account in the imperfect interface model which is a generalization of the Young–Laplace equation [see, e.g. 105]. In this simulation, we negled also the bending stiffness of graphene which could be considered extremely low [106, 107]. The wrinkling of graphene also induces a decrease in the GNP conductivity due to the presence of midgap state [108]. Here, we also find the conflicts between stiffness and conductivity. The influence of these geometric changes on the yield stress and toughness of the GNP polymer nanocomposite is not obvious. In our opinion, it would merit special study because of deformation mechanism such as cavitation [17] or crazing [91]. The Table 3 summarizes all the conclusions resulting from this discussion, giving the supposed influence of changes in interface properties and geometry on the effective properties of GNP polymer nanocomposites.

5. Conclusion

In this paper, we have tackled the problem of identification of elastic continuum model by atomistic simulations for graphene polymer nanocomposite. The ALIAS method was developed to estimate the local stiffness tensor on all points of polymer graphene nanocomposite with a sandwich structure model. Results suggest that the graphene can be modeled at continuum scale by a general imperfect interface with zero thickness. The cohesive part of the general imperfect interface is very anistropic because the stiffness associated to the slip along graphene plane is five orders of magnitude lower than the stiffness associated to the opening mode perpendicular to the graphene. Moreover, the identification procedure revealed the existence of interphase on either side of the graphene with a thickness of 1 nm, which is one and a half times stiffer than the polymer bulk matrix.

The identified continuum model has been used to study the effective elastic properties of nanocomposites with sandwich microstructure by numerical homogenization. This study at continuum scale showed a softening effect due to the very low stiffness of slips along graphene plane is preponderant in relation to the interphase stiffening. Finally, the continuum model suggests that the wrinkling of graphene increases the stiffness of nanocomposites, as well as the increasing of interfacial cohesion by chemical route such as grafting of graphene.

Aknowledgements

X. Lu thanks the financial support of China Scholarship Council(CSC) for the Ph.D. thesis. The molecular simulations were carried out using the LAMMPS molecular dynamics software [109].

References

[1] G. Van Lier, C. Van Alsenoy, V. Van Doren, and P. Geerlings. Ab initio study of the elastic properties of single-walled carbon nanotubes and graphene. *Chem. Phys. Lett.*, 326(1):181–185, 2000.

[2] C. Lee, X. Wei, J. W. Kysar, and J. Hone. Measurement of the elastic properties and intrinsic strength of monolayer graphene. *Science*, 321(5887):385–388, 2008.

[3] D. Cai, K. Yusoh, and M. Song. The mechanical properties and morphology of a graphite oxide nanoplatelet/polyurethane composite. *Nanotechnology*, 20(8):085712, 2009.

[4] M. A. Rafiee, J. Rafiee, Z. Wang, H. Song, Z. Z. Yu, and N. Koratkar. Enhanced mechanical properties of nanocomposites at low graphene content. *ACS Nano*, 3(12):3884–3890, 2009.

[5] R. Verdejo, M. M. Bernal, L. J. Romasanta, and M. A. Lopez-Manchado. Graphene filled polymer nanocomposites. *J. Mater. Chem.*, 21(10):3301–3310, 2011.

[6] Y. T. Park, Y. Qian, C. Chan, T. Suh, M. G. Nejhad, Ch. W. Macosko, and A. Stein. Epoxy toughening with low graphene loading. *Advanced Functional Materials*, 25(4):575–585, 2015.

[7] X. Zhao, Q. Zhang, D. Chen, and P. Lu. Enhanced mechanical properties of graphene-based poly (vinyl alcohol) composites. *Macromolecules*, 43(5):2357–2363, 2010.

[8] M. Terrones, O. Martín, M. González, J. Pozuelo, B. Serrano, J. C. Cabanelas, S. M. Vega-Díaz, and J. Baselga. Interphases in graphene polymer-based nanocomposites: achievements and challenges. *Adv. Mater.*, 23(44):5302–5310, 2011.

[9] L. C. Tang, Y. J. Wan, D. Yan, Y. B. Pei, L. Zhao, Y. B. Li, L. B. Wu, J. X. Jiang, and G. Q. Lai. The effect of graphene dispersion on the mechanical properties of graphene/epoxy composites. *Carbon*, 60:16–27, 2013.

[10] I. Zaman, T. T. Phan, H.-C. Kuan, Q. Meng, L. T. B. La, L. Luong, O. Youssf, and J. Ma. Epoxy/graphene platelets nanocomposites with two levels of interface strength. *Polymer*, 52(7):1603–1611, 2011.

[11] C. Wan and B. Chen. Reinforcement and interphase of polymer/graphene oxide nanocomposites. *J. Mater. Chem.*, 22(8):3637–3646, 2012.
[12] J. Ma, Q. Meng, A. Michelmore, N. Kawashima, Z. Izzuddin, C. Bengtsson, and H.-C. Kuan. Covalently bonded interfaces for polymer/graphene composites. *J. Mater. Chem. A*, 1(13):4255–4264, 2013.
[13] L. Gong, I. A. Kinloch, R. J. Young, I. Riaz, R. Jalil, and K. S. Novoselov. Interfacial stress transfer in a graphene monolayer nanocomposite. *Adv. Mater.*, 22(24):2694–2697, 2010.
[14] H.-B. Zhang, W.-G. Zheng, Q. Yan, Z.-G. Jiang, and Z.-Z. Yu. The effect of surface chemistry of graphene on rheological and electrical properties of polymethylmethacrylate composites. *Carbon*, 50(14):5117–5125, 2012.
[15] Y. Liu, A.-L. Hamon, P. Haghi-Ashtiani, T. Reiss, B. Fan, D. He, and J. Bai. Quantitative study of interface/interphase in epoxy/graphene-based nanocomposites by combining STEM and EELS. *ACS Appl. Mater. Inter.*, 8(49):34151–34158, 2016.
[16] D. Brown, P. Mele, S. Marceau, and N. D. Alberola. A molecular dynamics study of a model nanoparticle embedded in a polymer matrix. *Macromolecules*, 36(4):1395–1406, 2003.
[17] C. Li, A. R. Browning, S. Christensen, and A. Strachan. Atomistic simulations on multilayer graphene reinforced epoxy composites. *Compos. Part A-Appl. S.*, 43(8):1293–1300, 2012.
[18] R. Rahman and A. Haque. Molecular modeling of crosslinked graphene-epoxy nanocomposites for characterization of elastic constants and interfacial properties. *Compos. Part B-Eng.*, 54:353–364, 2013.
[19] A. N. Rissanou and V. Harmandaris. Dynamics of various polymer–graphene interfacial systems through atomistic molecular dynamics simulations. *Soft Matter*, 10(16):2876–2888, 2014.
[20] J. Moon, S. Yang, and M. Cho. Interfacial strengthening between graphene and polymer through Stone-Thrower-Wales defects: Ab initio and molecular dynamics simulations. *Carbon*, 118:66–77, 2017.
[21] B. Mortazavi, J. Bardon, and S. Ahzi. Interphase effect on the elastic and thermal conductivity response of polymer nanocomposite materials: 3D finite element study. *Comp. Mater. Sci.*, 69:100–106, 2013.
[22] B. Mortazavi. *Multiscale modeling of thermal and mechanical properties of nanostructured materials and polymer nanocomposites*. PhD thesis, Université de Strasbourg, 2013.
[23] X. Lu, J. Yvonnet, F. Detrez, and J. Bai. Multiscale modeling of nonlinear electric conductivity in graphene-reinforced nanocomposites taking into account tunnelling effect. *J. Comput. Phys.*, 337:116–131, 2017.
[24] X. Lu. *Multiscale electro-mechanical modeling of graphene/polymer nanocomposites*. PhD thesis, Université Paris-Saclay, 2017.
[25] X. Lu, J. Yvonnet, F. Detrez, and J. Bai. Low electrical percolation thresholds and nonlinear effects in graphene-reinforced nanocomposites: a numerical analysis. *J. Compos. Mater.*, 52(20):2767–2775, 2018.
[26] S. C. Tjong. Structural and mechanical properties of polymer nanocomposites. *Mater. Sci. Eng., R*, 53(3-4):73–197, 2006.
[27] A. J. Crosby and J.-Y. Lee. Polymer nanocomposites: the "nano" effect on mechanical properties. *Polym. Rev.*, 47(2):217–229, 2007.
[28] R. D. Peng, H. W. Zhou, H. W. Wang, and L. Mishnaevsky Jr. Modeling of nano-reinforced polymer composites: Microstructure effect on Young's modulus. *Comp. Mater. Sci.*, 60:19–31, 2012.
[29] Z. Liu, J. A. Moore, and W. K. Liu. An extended micromechanics method for probing interphase properties in polymer nanocomposites. *J. Mech. Phys. Solids*, 95:663–680, 2016.
[30] H. Wan, F. Delale, and L. Shen. Effect of CNT length and CNT-matrix interphase in carbon nanotube (CNT) reinforced composites. *Mech. Res. Commun.*, 32(5):481–489, 2005.
[31] G. D. Seidel and D. C. Lagoudas. Micromechanical analysis of the effective elastic properties of carbon nanotube reinforced composites. *Mech. Mater.*, 38(8-10):884–907, 2006.
[32] A. Hernández-Pérez and F. Avilés. Modeling the influence of interphase on the elastic properties of carbon nanotube composites. *Comp. Mater. Sci.*, 47(4):926–933, 2010.
[33] S. Yang, S. Yu, J. Ryu, J.-M. Cho, W. Kyoung, D.-S. Han, and M. Cho. Nonlinear multiscale modeling approach to characterize elastoplastic behavior of CNT/polymer nanocomposites considering the interphase and interfacial imperfection. *Int. J. Plasticity*, 41:124–146, 2013.
[34] A. Srivastava and D. Kumar. A continuum model to study interphase effects on elastic properties of CNT/GS–nanocomposite. *Mater. Res. Express*, 4(2):025036, 2017.
[35] K. I. Tserpes, A. Chanteli, and I. S. Floros. Prediction of yield strength of MWCNT/PP nanocomposite considering the interphase and agglomeration. *Compos. Struct.*, 168:657–662, 2017.
[36] G. M. Odegard, T. C. Clancy, and T. S. Gates. Modeling of the mechanical properties of nanoparticle/polymer composites. *Polymer*, 46(2):553–562, 2005.
[37] V. Marcadon, D. Brown, E. Hervé, P. Mélé, N. D. Albérola, and A. Zaoui. Confrontation between molecular dynamics and micromechanical approaches to investigate particle size effects on the mechanical behaviour of polymer nanocomposites. *Comp. Mater. Sci.*, 79:495–505, 2013.
[38] T.-T. Le, J. Guilleminot, and Ch. Soize. Stochastic continuum modeling of random interphases from atomistic simulations. Application to a polymer nanocomposite. *Comput. Methods Appl. Mech. Engrg.*, 303:430–449, 2016.
[39] B. Kim, J. Choi, S. Yang, S. Yu, and M. Cho. Multiscale modeling of interphase in crosslinked epoxy nanocomposites. *Compos. Part B-Eng.*, 120:128–142, 2017.
[40] P. Bövik. On the modelling of thin interface layers in elastic and acoustic scattering problems. *Q. J. Mech. Appl. Math*, 47(1):17–42, 1994.
[41] M. E. Gurtin, J. Weissmüller, and F. Larche. A general theory of curved deformable interfaces in solids at equilibrium. *Philos. Mag. A*, 78(5):1093–1109, 1998.

[42] S.-T. Gu and Q.-C. He. Interfacial discontinuity relations for coupled multifield phenomena and their application to the modeling of thin interphases as imperfect interfaces. *J. Mech. Phys. Solids*, 59(7):1413–1426, 2011.
[43] Y. Benveniste. Models of thin interphases with variable moduli in plane-strain elasticity. *Math. Mech. Solids*, 18(2):119–134, 2013.
[44] S.-T. Gu, J.-T. Liu, and Q.-C. He. Size-dependent effective elastic moduli of particulate composites with interfacial displacement and traction discontinuities. *Int. J. Solids Struct.*, 51(13):2283–2296, 2014.
[45] G. Chatzigeorgiou, F. Meraghni, and A. Javili. Generalized interfacial energy and size effects in composites. *J. Mech. Phys. Solids*, 106:257–282, 2017.
[46] G. I. Barenblatt. The formation of equilibrium cracks during brittle fracture. general ideas and hypotheses. Axially-symmetric cracks. *J. Appl. Math. Mech.-USS*, 23(3):622–636, 1959.
[47] D. S. Dugdale. Yielding of steel sheets containing slits. *J. Mech. Phys. Solids*, 8(2):100–104, 1960.
[48] M. E. Gurtin and A. I. Murdoch. A continuum theory of elastic material surfaces. *Arch. Ration. Mech. An.*, 57(4):291–323, 1975.
[49] A. I. Murdoch. A thermodynamical theory of elastic material interfaces. *Q. J. Mech. Appl. Math*, 29(3):245–275, 1976.
[50] E. N. Skountzos, A. Anastassiou, V. G. Mavrantzas, and D. N. Theodorou. Determination of the mechanical properties of a poly(methyl methacrylate) nanocomposite with functionalized graphene sheets through detailed atomistic simulations. *Macromolecules*, 47(22):8072–8088, 2014.
[51] J. Fan, A. Anastassiou, Ch. W. Macosko, and E. B. Tadmor. Molecular dynamics predictions of thermomechanical properties of an epoxy thermosetting polymer. *Polymer*, 196:122477, 2020.
[52] V. B. Shenoy. Atomistic calculations of elastic properties of metallic fcc crystal surfaces. *Phys. Rev. B*, 71(9):094104, 2005.
[53] H. S. Park, P. A. Klein, and G. J. Wagner. A surface Cauchy-Born model for nanoscale materials. *Int. J. Numer. Meth. Engng.*, 68(10):1072–1095, 2006.
[54] J. Yvonnet, A. Mitrushchenkov, G. Chambaud, and Q.-C. He. Finite element model of ionic nanowires with size-dependent mechanical properties determined by ab initio calculations. *Comput. Methods Appl. Mech. Engrg.*, 200(5-8):614–625, 2011.
[55] J. Yvonnet, A. Mitrushchenkov, G. Chambaud, Q.-C. He, and S.-T. Gu. Characterization of surface and nonlinear elasticity in wurtzite ZnO nanowires. *J. Appl. Phys.*, 111(12):124305, 2012.
[56] D. Davydov, A. Javili, and P. Steinmann. On molecular statics and surface-enhanced continuum modeling of nano-structures. *Comp. Mater. Sci.*, 69:510–519, 2013.
[57] D. Davydov, A. Javili, P. Steinmann, and A. McBride. A comparison of atomistic and surface enhanced continuum approaches at finite temperature. In *Surface Effects in Solid Mechanics*, pages 43–57. Springer, 2013.
[58] M. T. Hoang, J. Yvonnet, A. Mitrushchenkov, G. Chambaud, and H. L. Duan. Size-dependent mechanical properties of axial and radial mixed AlN/GaN nanostructure. *Nanotechnology*, 26(11):115703, 2015.
[59] B. A. M. Elsner, S. Müller, S. Bargmann, and J. Weissmüller. Surface excess elasticity of gold: Ab initio coefficients and impact on the effective elastic response of nanowires. *Acta Materialia*, 124:468–477, 2017.
[60] S. Namilae and N. Chandra. Multiscale model to study the effect of interfaces in carbon nanotube-based composites. *J. Eng. Mater.-T ASME*, 127(2):222–232, 2005.
[61] W. B. Lu, J. Wu, L. Y. Jiang, Y. Huang, K. C. Hwang, and B. Liu. A cohesive law for multi-wall carbon nanotubes. *Philos. Mag.*, 87(14-15):2221–2232, 2007.
[62] A. P. Awasthi, D. C. Lagoudas, and D. C. Hammerand. Modeling of graphene-polymer interfacial mechanical behavior using molecular dynamics. *Modell. Simul. Mater. Sci. Eng.*, 17(1):015002, 2008.
[63] Y. J. Liu, N. Nishimura, D. Qian, N. Adachi, Y. Otani, and V. Mokashi. A boundary element method for the analysis of CNT/polymer composites with a cohesive interface model based on molecular dynamics. *Eng. Anal. Bound. Elem.*, 32(4):299–308, 2008.
[64] Y. Chen, J. Y. H. Chia, Z. C. Su, T. E. Tay, and V. B. C. Tan. Mechanical characterization of interfaces in epoxy-clay nanocomposites by molecular simulations. *Polymer*, 54(2):766–773, 2013.
[65] S. Song, Y. Chen, Z. Su, C. Quan, and V. B. C. Tan. Multiscale modeling of damage progression in nylon 6/clay nanocomposites. *Compos. Sci. Technol.*, 100:189–197, 2014.
[66] B. Paliwal, W. B. Lawrimore, M. Q. Chandler, and M. F. Horstemeyer. Nanomechanical modeling of interfaces of polyvinyl alcohol (PVA)/clay nanocomposite. *Philos. Mag.*, 97(15):1179–1208, 2017.
[67] K. Liao and S. Li. Interfacial characteristics of a carbon nanotube–polystyrene composite system. *Appl. Phys. Lett.*, 79(25):4225–4227, 2001.
[68] J. Gou, B. Minaie, B. Wang, Z. Liang, and C. Zhang. Computational and experimental study of interfacial bonding of single-walled nanotube reinforced composites. *Comp. Mater. Sci.*, 31(3-4):225–236, 2004.
[69] L. Y. Jiang, Y. Huang, H. Jiang, G. Ravichandran, H. Gao, K. C. Hwang, and B. Liu. A cohesive law for carbon nanotube/polymer interfaces based on the van der Waals force. *J. Mech. Phys. Solids*, 54(11):2436–2452, 2006.
[70] S. C. Chowdhury and T. Okabe. Computer simulation of carbon nanotube pull-out from polymer by the molecular dynamics method. *Compos. Part A-Appl. S.*, 38(3):747–754, 2007.
[71] E. B Tadmor and R. E Miller. *Modeling materials: continuum, atomistic and multiscale techniques*. Cambridge University Press, 2011.
[72] S. Li and X.-L. Gao. *Handbook of micromechanics and nanomechanics*. CRC Press, 2013.
[73] S. Pfaller, M. Rahimi, G. Possart, P. Steinmann, F. Müller-Plathe, and M. C. Böhm. An Arlequin-based method to couple molecular dynamics and finite element simulations of amorphous polymers and nanocomposites. *Comput. Methods Appl. Mech. Engrg.*, 260:109–129, 2013.
[74] S. Pfaller, G. Possart, P. Steinmann, M. Rahimi, F. Müller-Plathe, and M. C. Böhm. Investigation of interphase effects

in silica-polystyrene nanocomposites based on a hybrid molecular-dynamics–finite-element simulation framework. *Phys. Rev. E*, 93(5):052505, 2016.
[75] S. Pfaller, A. Kergaßner, and P. Steinmann. Optimisation of the Capriccio method to couple particle-and continuum-based simulations of polymers. *Multiscale Sci. Eng.*, 1(4):318–333, 2019.
[76] A. I. Murdoch. *Physical Foundations of Continuum Mechanics*. Cambridge, 2012.
[77] M. Born. On the stability of crystal lattices I. *Math. Proc. Cambridge Philos. Soc.*, 36(2):160–172, 1940.
[78] J. H. Weiner. Hellmann-Feynman theorem, elastic moduli, and the Cauchy relations. *Phys. Rev. B*, 24(2):845, 1981.
[79] M. Arroyo and T. Belytschko. An atomistic-based finite deformation membrane for single layer crystalline films. *J. Mech. Phys. Solids*, 50(9):1941–1977, 2002.
[80] M. Arroyo and T. Belytschko. Finite crystal elasticity of carbon nanotubes based on the exponential Cauchy-Born rule. *Phys. Rev. B*, 69(11):115415, 2004.
[81] A. Tanguy, J. P. Wittmer, F. Leonforte, and J. L. Barrat. Continuum limit of amorphous elastic bodies: a finite-size study of low-frequency harmonic vibrations. *Phys. Rev. B*, 66(17):174205, 2002.
[82] J. P. Wittmer, A. Tanguy, J. L. Barrat, and L. Lewis. Vibrations of amorphous, nanometric structures: When does continuum theory apply? *Europhys. Lett.*, 57(3):423, 2002.
[83] C. Maloney and A. Lemaître. Universal breakdown of elasticity at the onset of material failure. *Phys. Rev. Lett.*, 93(19):195501, 2004.
[84] C. Maloney and A. Lemaître. Amorphous systems in athermal, quasistatic shear. *Phys. Rev. E*, 74(1):016118, 2006.
[85] A. Lemaître and C. Maloney. Sum rules for the quasi-static and visco-elastic response of disordered solids at zero temperature. *J. Stat. Phys.*, 123(2):415–452, 2006.
[86] K. Maeda and S. Takeuchi. Computer simulation of deformation in two-dimensional amorphous structures. *Phys. Status Solidi A*, 49(2):685–696, 1978.
[87] S. Kobayashi, K. Maeda, and S. Takeuchi. Computer simulation of deformation of amorphous Cu57Zr43. *Acta Metall.*, 28(12):1641–1652, 1980.
[88] K. Maeda and S. Takeuchi. Atomistic process of plastic deformation in a model amorphous metal. *Philos. Mag. A*, 44(3):643–656, 1981.
[89] A. Javili, P. Steinmann, and J. Mosler. Micro-to-macro transition accounting for general imperfect interfaces. *Comput. Methods Appl. Mech. Engrg.*, 317:274–317, 2017.
[90] A. Javili. A note on traction continuity across an interface in a geometrically non-linear framework. *Math. Mech. Solids*, page 1081286518766980, 2018.
[91] X. Lu, F. Detrez, J. Yvonnet, and J. Bai. Multiscale study of influence of interfacial decohesion on piezoresistivity of graphene/polymer nanocomposites. *Modell. Simul. Mater. Sci. Eng.*, 27(3):035001, 2019.
[92] S. L. Mayo, B. D. Olafson, and W. A. Goddard. DREIDING: a generic force field for molecular simulations. *J. Phys. Chem.*, 94(26):8897–8909, 1990.
[93] N. C. Admal and E. B. Tadmor. A unified interpretation of stress in molecular systems. *J. Elasticity*, 100(1):63–143, 2010.
[94] N. C. Admal and E. B. Tadmor. The non-uniqueness of the atomistic stress tensor and its relationship to the generalized beltrami representation. *J. Mech. Phys. Solids*, 93:72–92, 2016.
[95] N. C. Admal and E. B. Tadmor. Material fields in atomistics as pull-backs of spatial distributions. *J. Mech. Phys. Solids*, 89:59–76, 2016.
[96] M. Zhou. A new look at the atomic level virial stress: on continuum-molecular system equivalence. *P. Roy. Soc. Lond. A Mat.*, 459(2037):2347–2392, 2003.
[97] G. Gremaud. *Eulerian theory of newtonian deformable lattices-dislocation and disclination charges in solids*. EPFL-BOOK-220175, 2016.
[98] S.-T. Gu, E. Monteiro, and Q.-C. He. Coordinate-free derivation and weak formulation of a general imperfect interface model for thermal conduction in composites. *Compos. Sci. Technol.*, 71(9):1209–1216, 2011.
[99] J.-L. Halary, F. Lauprêtre, and L. Monnerie. *Polymer materials: macroscopic properties and molecular interpretations*, chapter Chapter 4 Secondary relaxations in amorphous polymers, pages 59–84. John Wiley & Sons, 2011.
[100] D. S. Fryer, R. D. Peters, E. J. Kim, J. E. Tomaszewski, J. J. De Pablo, P. F. Nealey, Ch. C. White, and W.-L. Wu. Dependence of the glass transition temperature of polymer films on interfacial energy and thickness. *Macromolecules*, 34(16):5627–5634, 2001.
[101] A. Bansal, H. Yang, C. Li, K. Cho, B. C. Benicewicz, S. K. Kumar, and L. S. Schadler. Quantitative equivalence between polymer nanocomposites and thin polymer films. *Nature materials*, 4(9):693–698, 2005.
[102] D. N. Theodorou and U. W. Suter. Atomistic modeling of mechanical properties of polymeric glasses. *Macromolecules*, 19(1):139–154, 1986.
[103] X. Chen and J. Li. Superlubricity of carbon nanostructures. *Carbon*, 158:1–23, 2020.
[104] R. O. Ritchie. The conflicts between strength and toughness. *Nat. Mater.*, 10(11):817–822, 2011.
[105] J. Yvonnet, H. Le Quang, and Q.-C. He. An XFEM/level set approach to modelling surface/interface effects and to computing the size-dependent effective properties of nanocomposites. *Comp. Mech.*, 42(1):119–131, 2008.
[106] Yujie Wei, Baoling Wang, Jiangtao Wu, Ronggui Yang, and Martin L Dunn. Bending rigidity and gaussian bending stiffness of single-layered graphene. *Nano letters*, 13(1):26–30, 2013.
[107] Banafsheh Sajadi, Simon van Hemert, Behrouz Arash, Pierpaolo Belardinelli, Peter G Steeneken, and Farbod Alijani. Size-and temperature-dependent bending rigidity of graphene using modal analysis. *Carbon*, 139:334–341, 2018.
[108] K. Xu, P. Cao, and J. R. Heath. Scanning tunneling microscopy characterization of the electrical properties of wrinkles in exfoliated graphene monolayers. *Nano Lett.*, 9(12):4446–4451, 2009.

[109] S. Plimpton. Fast parallel algorithms for short-range molecular dynamics. *J. Comput. Phys.*, 117(1):1–19, 1995.

Supplementary Information for : Identification of elastic properties of interphase and interface in graphene-polymer nanocomposites by atomistic simulations

Xiaoxin Lu[a], Fabrice Detrez[b], Julien Yvonnet[b], Jinbo Bai[c]

[a] *Shenzhen Institute of advanced electronic materials, Shenzhen Institutes of Advanced Technology, Chinese Academy of Sciences, Shenzhen 518103, P.R.China*
[b] *MSME, Univ Gustave Eiffel, CNRS UMR 8208, Univ Paris Est Creteil, F-77454 Marne-la-Vallée, France*
[c] *Université Paris-Saclay, CentraleSupélec, CNRS, Laboratoire de Mécanique des Sols, Structures et Matériaux (MSSMAT), 91190, Gif-sur-Yvette, France*

Abstract

This document provides supplementary information regarding:

1. Expressions of DREIDING potential in term of interatomic distance
2. Fitting details of the cohesive stiffness of interface $\mathbf{K}^s$
3. Computation of effective stiffness tensor by atomistic simulations
4. Computation of effective stiffness tensor by numerical homogenization
5. Expression of Young's modulus as function of angle θ

1. Expressions of DREIDING potential in term of interatomic distance

In the DREIDING potential [1], the interactions of all the atoms are described by the valence (or bonded) interactions and the nonbonded interactions. For convienent reasons, we consider only the van der Waals interactions in the nonbonded part of DREIDING potential, which is modeled by the Lennard-Jones 12-6 type expression

$$\mathcal{U}^{(vdw)}\left(\{\mathbf{r}_\alpha\}\right) = \sum_\alpha \sum_{\substack{\beta\neq\alpha,\\ r_{\alpha\beta}<r_c}} 4\epsilon_{\alpha\beta}\left[\left(\frac{\sigma_{\alpha\beta}}{r_{\alpha\beta}}\right)^{12} - \left(\frac{\sigma_{\alpha\beta}}{r_{\alpha\beta}}\right)^{6}\right] \tag{1}$$

where $\epsilon_{\alpha\beta}$ and $\sigma_{\alpha\beta}$ are parameters which depends on the atom types. For computational reasons, we use a cut off radius $r_c = 14.0$Å.

We assume that the valence interactions consist of bond stretch ($\mathcal{U}^{(s)}$, two-body), bond-angle bend ($\mathcal{U}^{(b)}$, three-body), dihedral angle torsion ($\mathcal{U}^{(tor)}$, four-body). In the

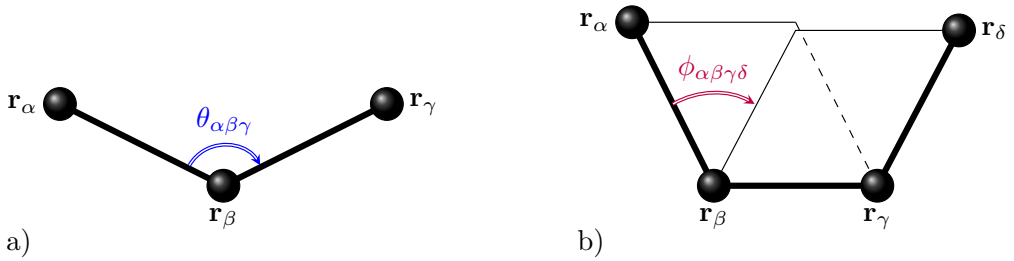

Figure 1: Definition of: a) the bending angle $\theta_{\alpha\beta\gamma}$ and b) the dihedral angle $\phi_{\alpha\beta\gamma\delta}$.

cas of coarse-grain PE and graphene, these potentials are written as

$$\mathcal{U}^{(s)}\left(\{\mathbf{r}_\alpha\}\right) = \sum_{\text{Bond}} \frac{k^{(s)}_{\alpha\beta}}{2}\left(r_{\alpha\beta} - r^0_{\alpha\beta}\right)^2, \tag{2}$$

$$\mathcal{U}^{(b)}\left(\{\mathbf{r}_\alpha\}\right) = \sum_{\text{Bending}} \frac{k^{(b)}_{\alpha\beta\gamma}}{2}\left(\cos\left(\theta_{\alpha\beta\gamma}\right) - \cos\left(\theta^0_{\alpha\beta\gamma}\right)\right)^2, \tag{3}$$

$$\mathcal{U}^{(tor)}\left(\{\mathbf{r}_\alpha\}\right) = \sum_{\text{Dihedral}} \frac{k^{(tor)}_{\beta\gamma}}{2}\left[1 - 3\cos\left(\phi_{\alpha\beta\gamma\delta}\right) + 4\cos^3\left(\phi_{\alpha\beta\gamma\delta}\right)\right], \tag{4}$$

where $k^{(s)}_{\alpha\beta}$, $r^0_{\alpha\beta}$, $k^{(b)}_{\alpha\beta\gamma}$, $\theta^0_{\alpha\beta\gamma}$ and $k^{(tor)}_{\beta\gamma}$ are parameters which depends on the atom types. The bending angle $\theta_{\alpha\beta\gamma}$ and the dihedral angle $\phi_{\alpha\beta\gamma\delta}$ are difened on Figure 1 and they can be computed using interatomic distances(see, e.g. [2] p. 468 for expression of dihedral angle cosine):

$$\cos\left(\theta_{\alpha\beta\gamma}\right) = \frac{\mathbf{r}_{\beta\alpha}.\mathbf{r}_{\beta\gamma}}{r_{\alpha\beta}r_{\beta\gamma}} = \frac{r^2_{\alpha\beta} + r^2_{\beta\gamma} - r^2_{\alpha\gamma}}{2r_{\alpha\beta}r_{\beta\gamma}}, \tag{5}$$

$$\cos\left(\phi_{\alpha\beta\gamma\delta}\right) = \frac{\left(\mathbf{r}_{\alpha\beta}\times\mathbf{r}_{\beta\gamma}\right)\cdot\left(\mathbf{r}_{\beta\gamma}\times\mathbf{r}_{\gamma\delta}\right)}{\left|\mathbf{r}_{\alpha\beta}\times\mathbf{r}_{\beta\gamma}\right|\left|\mathbf{r}_{\beta\gamma}\times\mathbf{r}_{\gamma\delta}\right|} \tag{6}$$

$$= \frac{\left(r^2_{\alpha\beta} + r^2_{\beta\gamma} - r^2_{\alpha\gamma}\right)\left(r^2_{\beta\gamma} + r^2_{\gamma\delta} - r^2_{\beta\delta}\right) - 2r^2_{\beta\gamma}\left(r^2_{\beta\gamma} - r^2_{\alpha\gamma} - r^2_{\beta\delta} + r^2_{\alpha\delta}\right)}{4\sqrt{r^2_{\alpha\beta}r^2_{\beta\gamma} - \frac{1}{4}\left(r^2_{\alpha\beta} + r^2_{\beta\gamma} - r^2_{\alpha\gamma}\right)^2}\sqrt{r^2_{\gamma\delta}r^2_{\beta\gamma} - \frac{1}{4}\left(r^2_{\gamma\delta} + r^2_{\beta\gamma} - r^2_{\beta\delta}\right)^2}}. \tag{7}$$

The total potential energy of the system is represented by the sum of all these contributions:

$$\mathcal{U}\left(\{\mathbf{r}_\alpha\}, \bar{\epsilon}\right) = \mathcal{U}^{(vdw)}\left(\{\mathbf{r}_\alpha\}\right) + \mathcal{U}^{(s)}\left(\{\mathbf{r}_\alpha\}\right) + \mathcal{U}^{(b)}\left(\{\mathbf{r}_\alpha\}\right) + \mathcal{U}^{(tor)}\left(\{\mathbf{r}_\alpha\}\right). \tag{8}$$

2. Fitting details of the cohesive stiffness of interface $\mathbf{K}^s$

The variation of potential energy $\Delta\mathcal{U}$ of the atomistic box for a translation $\mathbf{d}$ of graphene is quadratic form given by

$$\Delta\mathcal{U} = 2S\left(\mathbf{d}-\mathbf{d}_0\right)\ \cdot\ \mathbf{K}^s\ \cdot\ \left(\mathbf{d}-\mathbf{d}_0\right) \tag{9}$$

where S is the graphene sheet surface and $\mathbf{d}_0$ a small shift vector to correct the numerical error due to the numerical minimization of the initial configuration of atomistic box. The cohesive stiffness of interface $\mathbf{K}^s$ and the shift vector $\mathbf{d}_0$ matrix tensor $\mathbf{K}^s$ is defined by the least squares method, for a given set of $K = 37$ translations $\mathbf{d}^{(k)}$, such as

$$\{\mathbf{K}^s, \mathbf{d}_0\} = \underset{\mathbf{K}^s\in\mathcal{M}_3^{diag},\mathbf{d}_0\in\mathbb{R}^3}{\operatorname{argmin}} \left\{\sum_{k=1}^{K}\left|\Delta\mathcal{U}^{(k)} - 2S\left(\mathbf{d}^{(k)}-\mathbf{d}_0\right)\ \cdot\ \mathbf{K}^s\ \cdot\ \left(\mathbf{d}^{(k)}-\mathbf{d}_0\right)\right|^2\right\} \tag{10}$$

where $\mathcal{M}_3^{diag}$ is the set of diagonal matrix in basis $(\mathbf{e}_1, \mathbf{e}_2, \mathbf{e}_3)$ and $\Delta\mathcal{U}^{(k)}$ is the variation of potential energy for the translation $\mathbf{d}^{(k)}$. The 37 values of translation vector are chosen along six directions of translation $\{\mathbf{e}_1, \mathbf{e}_2, \mathbf{e}_3, \mathbf{e}_2+\mathbf{e}_3, \mathbf{e}_3+\mathbf{e}_1, \mathbf{e}_1+\mathbf{e}_2\}$. The Figure 2 shows the atomistic value of the variation of potential energy $\Delta\mathcal{U}$ and the quadratic fit for a translation into graphene plane along $\mathbf{e}_1$ and another one perpendicular to graphene plane $\mathbf{e}_3$). The cohesive part of the general imperfect interface is very anistropic because the stiffness associated to the opening mode perpendicular to the graphene $\mathbf{K}^s_{33} = 52960$ MPa.nm^{-1} is five order of magnitude than the stiffness associated to the slips along graphene plane $\mathbf{K}^s_{11} = \mathbf{K}^s_{22} = 8.50$ MPa.nm^{-1}.

3. Computation of effective stiffness tensor by atomistic simulations

The method presented in the previous section is a transposition of the procedure introduced by Theodorou and Suter [3] to estimate the stiffness tensor of polymer based materials. The starting point of this procedure is to write the variation of the total free energy $\Delta\overline{\phi}$ as function of the effective infinitesimal strain tensor $\overline{\boldsymbol{\epsilon}}$, such as

$$\Delta\overline{\phi} = \frac{|\Omega|}{2}\overline{\boldsymbol{\epsilon}} : \overline{\mathbb{C}}_A : \overline{\boldsymbol{\epsilon}} \tag{11}$$

Assuming that the temperature is 0 K in our simulations, the variation of free energy for a prescibed effectice strain $\overline{\boldsymbol{\epsilon}}$ is given by the variation of potential energy

$$\Delta\overline{\phi} = \Delta\mathcal{U} = \mathcal{U}\left(\overline{\boldsymbol{\epsilon}}\right) - \mathcal{U}\left(\mathbf{0}\right) \tag{12}$$

The effective stiffness $\overline{\mathbb{C}}_A$ is defined by the least squares method, for a given set of $K = 43$ effective strain $\overline{\boldsymbol{\epsilon}}^{(k)}$, such as

$$\overline{\mathbb{C}}_A = \underset{\overline{\mathbb{C}}_A\in\mathbb{O}\mathrm{rth}}{\operatorname{argmin}} \left\{\sum_{k=1}^{K}\left|\Delta\mathcal{U}^{(k)} - \frac{|\Omega|}{2}\overline{\boldsymbol{\epsilon}}^{(k)} : \overline{\mathbb{C}}_A : \overline{\boldsymbol{\epsilon}}^{(k)}\right|^2\right\} \tag{13}$$

where $\mathbb{O}$rth is the set of fourth order elastic tensor for orthorhombic material in basis $(\mathbf{e}_1, \mathbf{e}_2, \mathbf{e}_3)$ and $\Delta\mathcal{U}^{(k)}$ is the variation of potential energy for the prescribe effective strain

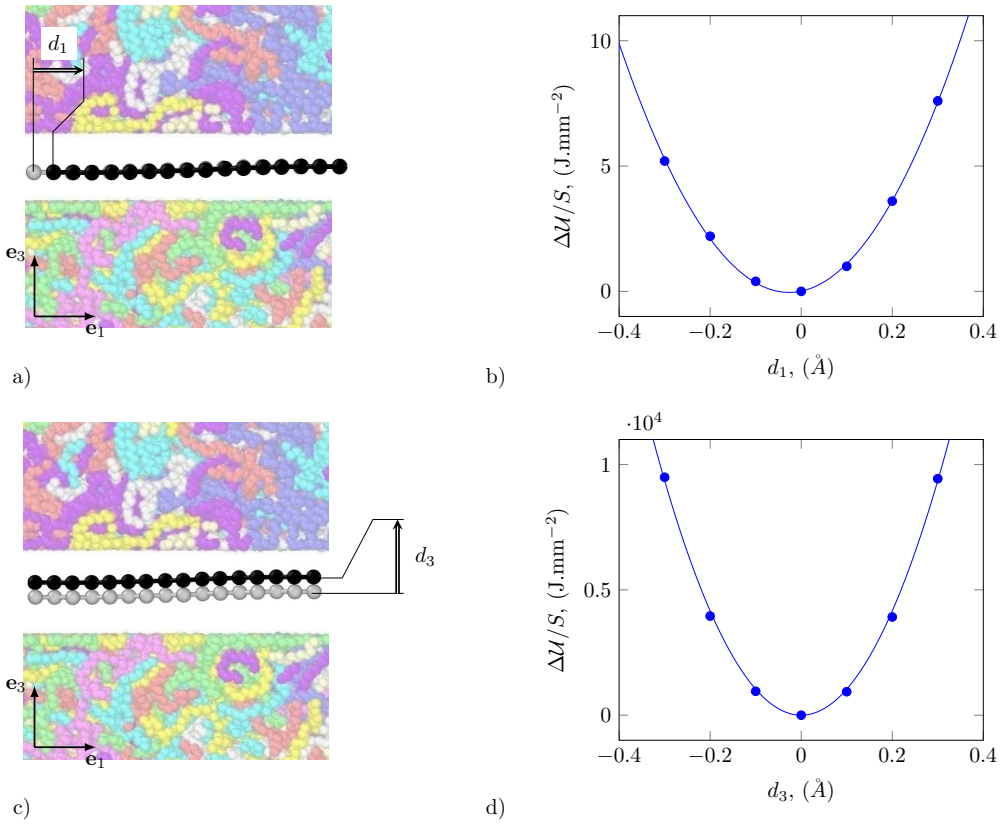

Figure 2: a) Scheme of graphene sheet translation along $\mathbf{e}_1$. b) Evolution of potential energy as function of d for translation of graphene along $\mathbf{e}_1$. c) Scheme of graphene sheet translation along $\mathbf{e}_3$. d) Evolution of potential energy as function of d_3 for translation of graphene along $\mathbf{e}_3$.

$\bar{\boldsymbol{\epsilon}}^{(k)}$. Note that this method is not limited to orthorhombic material, this simplifying assumption that guided by laminate geometry of atomistic box allowed us to reduce the coefficient number of $\overline{\mathbb{C}}_A$ from 21 to 9 $((\overline{\mathbb{C}}_A)_{11}, (\overline{\mathbb{C}}_A)_{22}, (\overline{\mathbb{C}}_A)_{33}, (\overline{\mathbb{C}}_A)_{44}, (\overline{\mathbb{C}}_A)_{55}, (\overline{\mathbb{C}}_A)_{66}$, $(\overline{\mathbb{C}}_A)_{12}, (\overline{\mathbb{C}}_A)_{23}, (\overline{\mathbb{C}}_A)_{31})$. Moreover, the elastic constant $(\overline{\mathbb{C}}_A)_{44}$ and $(\overline{\mathbb{C}}_A)_{55}$ cannot be obtained by atomistic simulations because of the sliding at the polymer/graphene interface, so we impose $(\overline{\mathbb{C}}_A)_{44} = (\overline{\mathbb{C}}_A)_{55} = 0$. The 43 values of effective strain $\bar{\boldsymbol{\epsilon}}^{(k)}$ are chossen along seven directions $\boldsymbol{\alpha}^{(j)}$ in space of symetric second order tensor $\{\mathbf{e}_1 \otimes \mathbf{e}_1$, $\mathbf{e}_2 \otimes \mathbf{e}_2$, $\mathbf{e}_3 \otimes \mathbf{e}_3$, $\frac{1}{\sqrt{2}}(\mathbf{e}_1 \otimes \mathbf{e}_2 + \mathbf{e}_2 \otimes \mathbf{e}_1)$, $\frac{1}{\sqrt{2}}(\mathbf{e}_1 \otimes \mathbf{e}_1 + \mathbf{e}_2 \otimes \mathbf{e}_2)$, $\frac{1}{\sqrt{2}}(\mathbf{e}_2 \otimes \mathbf{e}_2 + \mathbf{e}_3 \otimes \mathbf{e}_3)$, $\frac{1}{\sqrt{2}}(\mathbf{e}_3 \otimes \mathbf{e}_3 + \mathbf{e}_1 \otimes \mathbf{e}_1)\Big\}$. For each direction $\boldsymbol{\alpha}^{(j)}$, we prescribe six effective strains, such as

$$\bar{\boldsymbol{\epsilon}}^{(k)} = \lambda_i \boldsymbol{\alpha}^{(j)}, \qquad k = i + 7\,(j-1) \tag{14}$$

with $\lambda_i = \{-0.015; -0.01; -0.005; 0.005; 0.01; 0.015\}$

The effective stiffness tensor computes by atomistic simulations is

$$\overline{\mathbb{C}}_A = \begin{bmatrix} 43.3 & 18.7 & 8.8 & 0.0 & 0.0 & 0.0 \\ 18.7 & 43.3 & 8.8 & 0.0 & 0.0 & 0.0 \\ 8.8 & 8.8 & 14.1 & 0.0 & 0.0 & 0.0 \\ 0.0 & 0.0 & 0.0 & 0.0 & 0.0 & 0.0 \\ 0.0 & 0.0 & 0.0 & 0.0 & 0.0 & 0.0 \\ 0.0 & 0.0 & 0.0 & 0.0 & 0.0 & 12.3 \end{bmatrix} \text{ GPa} \tag{15}$$

4. Computation of effective stiffness tensor by numerical homogenization

In this section, the definition and computation of effective properties in the context of linear elasticity with imperfect interface are presented. The practical calculation of the effective elastic tensor with 3D Finite Element Method (FEM) is detailed. An overview of computational homogenization with FEM can be found in [4].

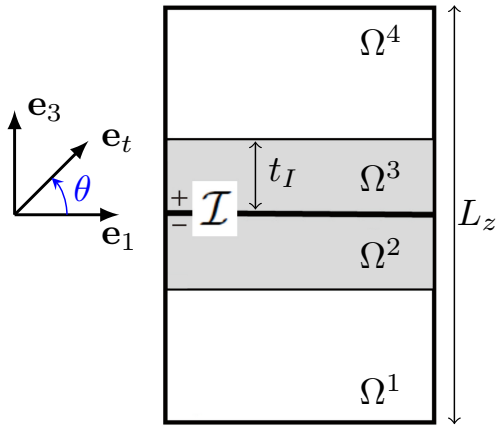

Figure 3: Representative Volume Element for periodic laminate polymer/graphene nanocomposte (L_z = 10 nm).

The Representative Volume Element (RVE) for periodic laminate polymer/graphene nanocomposte is composed by a five layers: an imperfect interface for graphene ($\mathcal{I}$), two interphase layers (Ω^2 and Ω^3) with a thickness, $t_I = 10.5$ Å and two layers for polymer bulk (Ω^1 and Ω^4) see Figure 3.

The continuum homogenization problem being linear, the effective stiffness of polymer/graphene nanocomposite $\overline{\mathbb{C}}_C$ given the macroscopic constitutive relationship betwen macro stress $\overline{\boldsymbol{\sigma}}$ and macro strain $\overline{\boldsymbol{\epsilon}}$

$$\overline{\boldsymbol{\sigma}} = \overline{\mathbb{C}}_C : \overline{\boldsymbol{\epsilon}} \tag{16}$$

is obtained by computing the macro stress for six elementary localization problems on

RVE with the following prescribed macro strains :

$$\begin{aligned} \overline{\boldsymbol{\epsilon}}^{(1)} &= \mathbf{e}_1 \otimes \mathbf{e}_1; & \overline{\boldsymbol{\epsilon}}^{(4)} &= 2\left(\mathbf{e}_2 \otimes \mathbf{e}_3 + \mathbf{e}_3 \otimes \mathbf{e}_2\right); \\ \overline{\boldsymbol{\epsilon}}^{(2)} &= \mathbf{e}_2 \otimes \mathbf{e}_2; & \overline{\boldsymbol{\epsilon}}^{(5)} &= 2\left(\mathbf{e}_3 \otimes \mathbf{e}_1 + \mathbf{e}_1 \otimes \mathbf{e}_3\right); \\ \overline{\boldsymbol{\epsilon}}^{(3)} &= \mathbf{e}_3 \otimes \mathbf{e}_3; & \overline{\boldsymbol{\epsilon}}^{(6)} &= 2\left(\mathbf{e}_1 \otimes \mathbf{e}_2 + \mathbf{e}_2 \otimes \mathbf{e}_1\right). \end{aligned} \tag{17}$$

4.1. Strong form

The localization problem based assuming that the RVE is subjected to the prediodic boundary condition is given as follows:

Given a macroscopic strain $\overline{\boldsymbol{\epsilon}}$, find the displacement field $\mathbf{u}(\mathbf{x})$ in Ω such that:

$$\nabla \cdot \boldsymbol{\sigma} = \mathbf{0} \qquad \forall \mathbf{x} \in \Omega, \tag{18}$$

$$\nabla^s \cdot \boldsymbol{\sigma}^s + [\![\mathbf{t}]\!] = \mathbf{0} \qquad \forall \mathbf{x} \in \mathcal{I}, \tag{19}$$

$$\boldsymbol{\sigma} = \mathbb{C}(\mathbf{x}) : \boldsymbol{\epsilon}(\mathbf{x}) \qquad \forall \mathbf{x} \in \Omega, \tag{20}$$

$$\boldsymbol{\sigma}^s = \mathbb{C}^s(\mathbf{x}) : \boldsymbol{\epsilon}^s(\mathbf{x}) \qquad \forall \mathbf{x} \in \mathcal{I}, \tag{21}$$

$$\mathbf{t}^s = \frac{1}{2}\left(\boldsymbol{\sigma}|_{\mathcal{I}}^{+} + \boldsymbol{\sigma}|_{\mathcal{I}}^{-}\right) \cdot \mathbf{n}_{\mathcal{I}} = \mathbf{K}^s \cdot [\![\mathbf{u}]\!] \qquad \forall \mathbf{x} \in \mathcal{I}, \tag{22}$$

with the kinematic

$$\boldsymbol{\epsilon}(\mathbf{x}) = \frac{1}{2}\left(\nabla \mathbf{u}(\mathbf{x}) + \nabla \mathbf{u}^T(\mathbf{x})\right), \qquad \forall \mathbf{x} \in \Omega, \tag{23}$$

$$\boldsymbol{\epsilon}^s(\mathbf{x}) = \frac{1}{2}\left(\nabla^s \mathbf{u}^s(\mathbf{x}) + \left(\nabla^s \mathbf{u}^s(\mathbf{x})\right)^T\right) \qquad \forall \mathbf{x} \in \mathcal{I}, \tag{24}$$

$$\mathbf{u}^s(\mathbf{x}) = \frac{1}{2}\left(\mathbf{u}|_{\mathcal{I}}^{+} + \mathbf{u}|_{\mathcal{I}}^{-}\right) \qquad \forall \mathbf{x} \in \mathcal{I}, \tag{25}$$

$$[\![\mathbf{u}]\!] = \mathbf{u}|_{\mathcal{I}}^{+} - \mathbf{u}|_{\mathcal{I}}^{-} \qquad \forall \mathbf{x} \in \mathcal{I}. \tag{26}$$

and verifying the periodic boundary conditions

$$\mathbf{u}(\mathbf{x}) = \overline{\boldsymbol{\epsilon}} \cdot \mathbf{x} + \tilde{\mathbf{u}}(\mathbf{x}), \qquad \forall \mathbf{x} \in \partial\Omega \tag{27}$$

where the fluctuation $\tilde{\mathbf{u}}(\mathbf{x})$ is periodic on Ω and discoutinous over the imperfect interface $\mathcal{I}$. In other words, it takes the same values at two homologous points on opposite faces of a parallelepipedic domain Ω. The traction vectors $\boldsymbol{\sigma} \cdot \mathbf{n}$ and $\boldsymbol{\sigma}^s \cdot \mathbf{n}$ are antiperiodic.

4.2. Weak form

Given a macroscopic strain $\overline{\boldsymbol{\epsilon}}$, find $\tilde{\mathbf{u}} \in \mathcal{H}_1^p(\Omega)$ for all $\delta\mathbf{u} \in \mathcal{H}_1^p(\Omega)$, such as :

$$\int_\Omega \boldsymbol{\sigma}[\mathbf{u}] : \boldsymbol{\epsilon}[\delta\mathbf{u}] \, \mathrm{d}V + \int_{\mathcal{I}} \boldsymbol{\sigma}^s[\mathbf{u}] : \boldsymbol{\epsilon}^s[\delta\mathbf{u}] + \mathbf{t}^s[[\![\mathbf{u}]\!]] \cdot [\![\delta\mathbf{u}]\!] \, \mathrm{d}S = 0 \tag{28}$$

where $\mathbf{u} = \overline{\boldsymbol{\epsilon}} \cdot \mathbf{x} + \tilde{\mathbf{u}}$ and $\mathcal{H}_1^p(\Omega)$ is the set $\{\mathbf{w}(\mathbf{x})$ periodic on Ω and continous on $\Omega \backslash \mathcal{I}$, such as $\int_\Omega \mathbf{w}^2 \, \mathrm{d}V < \infty$, $\int_\Omega \nabla\mathbf{w} : \nabla\mathbf{w} \, \mathrm{d}V < \infty$ $\}$.

The equation (28) becomes after using the elastic constitutive laws

$$\int_{\Omega} \boldsymbol{\epsilon}\left[\tilde{\mathbf{u}}\right] : \mathbb{C}\left(\mathbf{x}\right) : \boldsymbol{\epsilon}\left[\delta\mathbf{u}\right] \, \mathrm{d}V + \int_{\mathcal{I}} \boldsymbol{\epsilon}^s\left[\tilde{\mathbf{u}}\right] : \mathbb{C}^s\left(\mathbf{x}\right) : \boldsymbol{\epsilon}^s\left[\delta\mathbf{u}\right] + [\![\tilde{\mathbf{u}}]\!] \cdot \mathbf{K}^s \cdot [\![\delta\mathbf{u}]\!] \, \mathrm{d}S \quad (29)$$
$$= -\int_{\Omega} \overline{\boldsymbol{\epsilon}} : \mathbb{C}\left(\mathbf{x}\right) : \boldsymbol{\epsilon}\left[\delta\mathbf{u}\right] \, \mathrm{d}V - \int_{\mathcal{I}} \overline{\boldsymbol{\epsilon}}^s : \mathbb{C}^s\left(\mathbf{x}\right) : \boldsymbol{\epsilon}^s\left[\delta\mathbf{u}\right] \, \mathrm{d}S$$

where $\overline{\boldsymbol{\epsilon}}^s = \mathbf{P} \cdot \overline{\boldsymbol{\epsilon}} \cdot \mathbf{P}$ is the projection of the macro strain onto the tangent plane of the interface $\mathcal{I}$ and $\mathbf{P} = \mathbf{I} - \mathbf{n}_{\mathcal{I}} \otimes \mathbf{n}_{\mathcal{I}}$.

4.3. Finite element discretization

For the discretization of this discontinous weak form it suffices to divide the domain into two subdomains, Ω^- and Ω^+, separated by the interface $\mathcal{I}$ and write the weak as follow :

Given a macroscopic strain $\overline{\boldsymbol{\epsilon}}$, find $\tilde{\mathbf{u}} \in \mathcal{H}_1^p(\Omega)$ for all $\delta\mathbf{u} \in \mathcal{H}_1^p(\Omega)$, such as :

$$m^{++}\left(\tilde{\mathbf{u}}, \delta\mathbf{u}\right) + m^{--}\left(\tilde{\mathbf{u}}, \delta\mathbf{u}\right) + m^{+-}\left(\tilde{\mathbf{u}}, \delta\mathbf{u}\right) + m^{-+}\left(\tilde{\mathbf{u}}, \delta\mathbf{u}\right) = f_{\overline{\boldsymbol{\epsilon}}}^{+}\left(\delta\mathbf{u}\right) + f_{\overline{\boldsymbol{\epsilon}}}^{-}\left(\delta\mathbf{u}\right) \quad (30)$$

where

$$\begin{aligned}
m^{++}\left(\tilde{\mathbf{u}}, \delta\mathbf{u}\right) &= \int_{\Omega^+} \boldsymbol{\epsilon}\left[\tilde{\mathbf{u}}\right] : \mathbb{C}\left(\mathbf{x}\right) : \boldsymbol{\epsilon}\left[\delta\mathbf{u}\right] \, \mathrm{d}V + \int_{\mathcal{I}^+} \frac{1}{4}\boldsymbol{\epsilon}^s\left[\tilde{\mathbf{u}}|_{\mathcal{I}}^{+}\right] : \mathbb{C}^s\left(\mathbf{x}\right) : \boldsymbol{\epsilon}^s\left[\delta\mathbf{u}|_{\mathcal{I}}^{+}\right] \, \mathrm{d}S \\
&\quad + \int_{\mathcal{I}^+} \tilde{\mathbf{u}}|_{\mathcal{I}}^{+} \cdot \mathbf{K}^s \cdot \delta\mathbf{u}|_{\mathcal{I}}^{+} \, \mathrm{d}S, \\
m^{--}\left(\tilde{\mathbf{u}}, \delta\mathbf{u}\right) &= \int_{\Omega^-} \boldsymbol{\epsilon}\left[\tilde{\mathbf{u}}\right] : \mathbb{C}\left(\mathbf{x}\right) : \boldsymbol{\epsilon}\left[\delta\mathbf{u}\right] \, \mathrm{d}V + \int_{\mathcal{I}^-} \frac{1}{4}\boldsymbol{\epsilon}^s\left[\tilde{\mathbf{u}}|_{\mathcal{I}}^{-}\right] : \mathbb{C}^s\left(\mathbf{x}\right) : \boldsymbol{\epsilon}^s\left[\delta\mathbf{u}|_{\mathcal{I}}^{-}\right] \, \mathrm{d}S \\
&\quad + \int_{\mathcal{I}^-} \tilde{\mathbf{u}}|_{\mathcal{I}}^{-} \cdot \mathbf{K}^s \cdot \delta\mathbf{u}|_{\mathcal{I}}^{-} \, \mathrm{d}S, \\
m^{+-}\left(\tilde{\mathbf{u}}, \delta\mathbf{u}\right) &= \int_{\mathcal{I}} \frac{1}{4}\boldsymbol{\epsilon}^s\left[\tilde{\mathbf{u}}|_{\mathcal{I}}^{+}\right] : \mathbb{C}^s\left(\mathbf{x}\right) : \boldsymbol{\epsilon}^s\left[\delta\mathbf{u}|_{\mathcal{I}}^{-}\right] \, \mathrm{d}S - \int_{\mathcal{I}} \tilde{\mathbf{u}}|_{\mathcal{I}}^{+} \cdot \mathbf{K}^s \cdot \delta\mathbf{u}|_{\mathcal{I}}^{-} \, \mathrm{d}S, \\
m^{-+}\left(\tilde{\mathbf{u}}, \delta\mathbf{u}\right) &= \int_{\mathcal{I}} \frac{1}{4}\boldsymbol{\epsilon}^s\left[\tilde{\mathbf{u}}|_{\mathcal{I}}^{-}\right] : \mathbb{C}^s\left(\mathbf{x}\right) : \boldsymbol{\epsilon}^s\left[\delta\mathbf{u}|_{\mathcal{I}}^{+}\right] \, \mathrm{d}S - \int_{\mathcal{I}} \tilde{\mathbf{u}}|_{\mathcal{I}}^{-} \cdot \mathbf{K}^s \cdot \delta\mathbf{u}|_{\mathcal{I}}^{+} \, \mathrm{d}S, \\
f_{\overline{\boldsymbol{\epsilon}}}^{+}\left(\delta\mathbf{u}\right) &= -\int_{\Omega^+} \overline{\boldsymbol{\epsilon}} : \mathbb{C}\left(\mathbf{x}\right) : \boldsymbol{\epsilon}\left[\delta\mathbf{u}\right] \, \mathrm{d}V - \int_{\mathcal{I}^+} \frac{1}{2}\overline{\boldsymbol{\epsilon}}^s : \mathbb{C}^s\left(\mathbf{x}\right) : \boldsymbol{\epsilon}^s\left[\delta\mathbf{u}|_{\mathcal{I}}^{+}\right] \, \mathrm{d}S, \\
f_{\overline{\boldsymbol{\epsilon}}}^{-}\left(\delta\mathbf{u}\right) &= -\int_{\Omega^-} \overline{\boldsymbol{\epsilon}} : \mathbb{C}\left(\mathbf{x}\right) : \boldsymbol{\epsilon}\left[\delta\mathbf{u}\right] \, \mathrm{d}V - \int_{\mathcal{I}^-} \frac{1}{2}\overline{\boldsymbol{\epsilon}}^s : \mathbb{C}^s\left(\mathbf{x}\right) : \boldsymbol{\epsilon}^s\left[\delta\mathbf{u}|_{\mathcal{I}}^{-}\right] \, \mathrm{d}S.
\end{aligned}$$

The bilinear form $m^{++}\left(\tilde{\mathbf{u}}, \delta\mathbf{u}\right)$ and the linear form $f_{\overline{\boldsymbol{\epsilon}}}^{+}\left(\delta\mathbf{u}\right)$ (reps. $m^{--}\left(\tilde{\mathbf{u}}, \delta\mathbf{u}\right)$ and $f_{\overline{\boldsymbol{\epsilon}}}^{-}\left(\delta\mathbf{u}\right)$) are discretized by Lagrangian finite-element method with linear tetrahedron P1-elements of subdomain Ω^+ (resp. Ω^-) and computed by Gauss quadrature of order 1 and order 2 for the term $\int_{\mathcal{I}^+} \tilde{\mathbf{u}}|_{\mathcal{I}}^{+} \cdot \mathbf{K}^s \cdot \delta\mathbf{u}|_{\mathcal{I}}^{+} \, \mathrm{d}S$ (resp. $\int_{\mathcal{I}^-} \tilde{\mathbf{u}}|_{\mathcal{I}}^{-} \cdot \mathbf{K}^s \cdot \delta\mathbf{u}|_{\mathcal{I}}^{-} \, \mathrm{d}S$). To compute the coupling term $m^{-+}\left(\tilde{\mathbf{u}}, \delta\mathbf{u}\right)$ and $m^{-+}\left(\tilde{\mathbf{u}}, \delta\mathbf{u}\right)$, we impose the same discretization of interface $\mathcal{I}$ for the domains Ω^+ ans Ω^-.

The using 3D meshes are plotted on Figure 4. The element size is chosen when the values of the components of the stiffness tensors $\overline{\mathbb{C}}_C$ changed by minus 0.1% when the

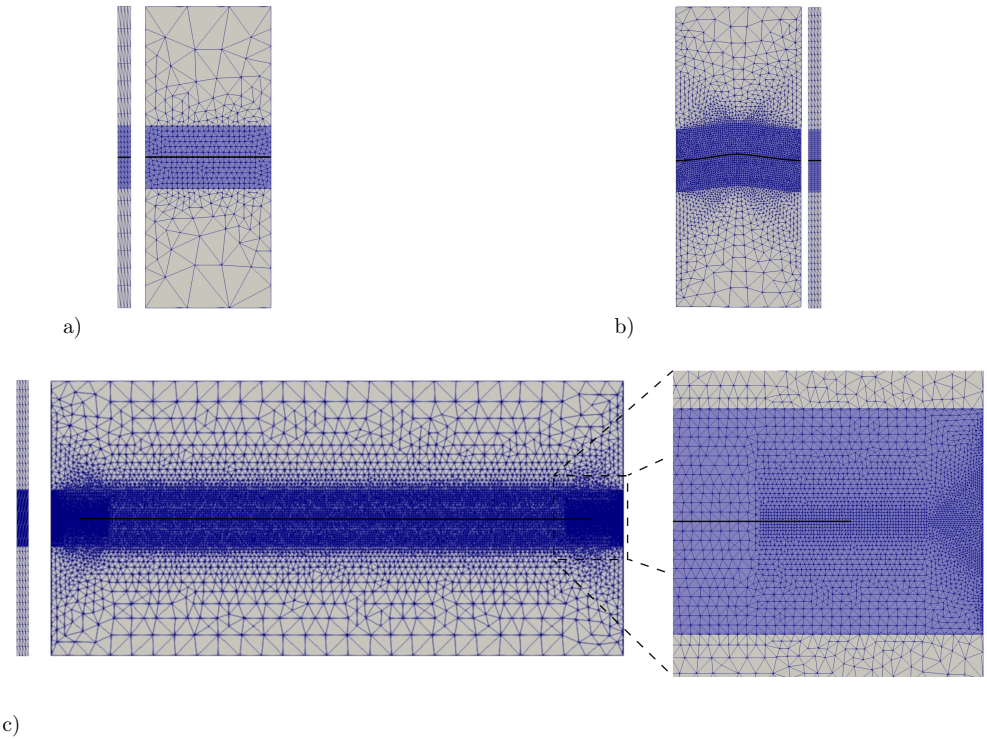

Figure 4: 3D meshes with linear tetrahedron P1-element of RVE whit : a) flat graphene, b) wrinkled graphene, c) finite size graphene.

number of degree of freedom (dof) is doubled. Note that the peridodic boundary conditions and the continuous translational symmetry of all RVE geometry along $\mathbf{e}_2$ (along $\mathbf{e}_1$ and $\mathbf{e}_2$ for flat graphene RVE) imply that the effective stiffness $\overline{\mathbb{C}}_C$ is independent of the lenght L_y for all studied RVE (and independent of L_x for flat graphene RVE). We chose $L_y = 4$Å with 4 rows of elements following the direction $\mathbf{e}_2$ to reduce the computational cost. The choice of L_x is arbitrary for all RVE while the $L_z = 10$ nm is chosen to have the same size as the atomic simulation box. The shape of wrinkled graphene is sinusoidal given by the parametric equations :

$$
\begin{aligned}
x &= u & u &\in \left[-\frac{L_x}{2}; \frac{L_x}{2}\right] \\
y &= v & v &\in \left[-\frac{L_y}{2}; \frac{L_y}{2}\right] \\
z &= \frac{\Delta}{2}\cos\left(2\pi\frac{u}{L_x}\right)
\end{aligned}
$$

where $\Delta = 2$Å and $L_x = 4$ nm. This choice gives the same order of magnitude graphene curvature that this one observed by dynamics molecular simulations at 300K [5].

Case of finite size graphene. In this case, we add a Neumman boundary condition at the interface border $\partial\mathcal{I}$, such as

$$\boldsymbol{\sigma}^s \cdot \mathbf{m} = \mathbf{0} \tag{31}$$

where $\mathbf{m}$ is the normal vector to the line $\partial\mathcal{I}$ and perpendicular to the normal unit vector of the interface $\mathbf{n}_\mathcal{I}$. Note that adding the boundary condition doesn't change the expresion of weak form (Eq. 28).

Case of wrinkled graphene. In this case, surface elastic parameter are express into the local basis $\mathcal{B}_\mathcal{I}[\mathbf{x}] = (\mathbf{t}_1[\mathbf{x}], \mathbf{t}_2[\mathbf{x}], \mathbf{n}_\mathcal{I}[\mathbf{x}])$

$$\begin{aligned}
\mathbb{C}^s(\mathbf{x}) =& \mathbb{C}^s_{11}\mathbf{t}_1[\mathbf{x}] \otimes \mathbf{t}_1[\mathbf{x}] \otimes \mathbf{t}_1[\mathbf{x}] \otimes \mathbf{t}_1[\mathbf{x}] \\
&+ \mathbb{C}^s_{22}\mathbf{t}_2[\mathbf{x}] \otimes \mathbf{t}_2[\mathbf{x}] \otimes \mathbf{t}_2[\mathbf{x}] \otimes \mathbf{t}_2[\mathbf{x}] \\
&+ \mathbb{C}^s_{12}(\mathbf{t}_1[\mathbf{x}] \otimes \mathbf{t}_1[\mathbf{x}] \otimes \mathbf{t}_2[\mathbf{x}] \otimes \mathbf{t}_2[\mathbf{x}] + \mathbf{t}_2[\mathbf{x}] \otimes \mathbf{t}_2[\mathbf{x}] \otimes \mathbf{t}_1[\mathbf{x}] \otimes \mathbf{t}_1[\mathbf{x}]) \\
&+ 2\mathbb{C}^s_{66}(\mathbf{t}_1[\mathbf{x}] \otimes \mathbf{t}_2[\mathbf{x}] + \mathbf{t}_2[\mathbf{x}] \otimes \mathbf{t}_1[\mathbf{x}]) \otimes (\mathbf{t}_1[\mathbf{x}] \otimes \mathbf{t}_2[\mathbf{x}] + \mathbf{t}_2[\mathbf{x}] \otimes \mathbf{t}_1[\mathbf{x}]),
\end{aligned} \tag{32}$$

$$\mathbf{K}^s(\mathbf{x}) = \mathbf{K}^s_{11}\mathbf{t}_1[\mathbf{x}] \otimes \mathbf{t}_1[\mathbf{x}] + \mathbf{K}^s_{22}\mathbf{t}_2[\mathbf{x}] \otimes \mathbf{t}_2[\mathbf{x}] + \mathbf{K}^s_{33}\mathbf{n}_\mathcal{I}[\mathbf{x}] \otimes \mathbf{n}_\mathcal{I}[\mathbf{x}], \tag{33}$$

where $\mathbb{C}^s_{ij}$ and $\mathbf{K}^s_{ii}$ are the corresponding components for the flat graphene case; and where $\mathbf{n}_\mathcal{I}[\mathbf{x}]$ is unit normal to the imperfect interface at point $\mathbf{x}$ and $(\mathbf{t}_1[\mathbf{x}], \mathbf{t}_2[\mathbf{x}])$ is the orthonormal basis of tangent plane to the imperfect interface at point $\mathbf{x}$. The vector $\mathbf{t}_2[\mathbf{x}] = \mathbf{e}_2 \ \forall \mathbf{x} \in \mathcal{I}$ because of the RVE is invariant by translation along $\mathbf{e}_2$.

4.4. Post-processing

The macro stress $\overline{\boldsymbol{\sigma}}$ defined by

$$\begin{aligned}
\overline{\boldsymbol{\sigma}} &= \frac{1}{|\Omega|}\int_\Omega \boldsymbol{\sigma}\,\mathrm{d}V + \frac{1}{|\Omega|}\int_\mathcal{I} \boldsymbol{\sigma}^s\,\mathrm{d}S \\
&= \frac{1}{|\Omega|}\int_{\Omega^+} \boldsymbol{\sigma}\,\mathrm{d}V + \frac{1}{|\Omega|}\int_{\Omega^-} \boldsymbol{\sigma}\,\mathrm{d}V \\
&\quad + \frac{1}{|\Omega|}\int_{\mathcal{I}^+} \frac{1}{2}\mathbb{C}^s(\mathbf{x}) : \boldsymbol{\epsilon}^s\left[\mathbf{u}|^+_\mathcal{I}\right]\,\mathrm{d}S + \frac{1}{|\Omega|}\int_{\mathcal{I}^-} \frac{1}{2}\mathbb{C}^s(\mathbf{x}) : \boldsymbol{\epsilon}^s\left[\mathbf{u}|^-_\mathcal{I}\right]\,\mathrm{d}S
\end{aligned} \tag{34}$$

is evaluated by Gauss quadrature of order 1.

The prescribed macro strain are chosen the Voigt's tensors basis so the effective stiffness tensor is given in Voigt notation by :

$$\overline{\mathbb{C}}_C = \left[\left[\overline{\boldsymbol{\sigma}}^{(1)}\right]; \left[\overline{\boldsymbol{\sigma}}^{(2)}\right]; \left[\overline{\boldsymbol{\sigma}}^{(3)}\right]; \left[\overline{\boldsymbol{\sigma}}^{(4)}\right]; \left[\overline{\boldsymbol{\sigma}}^{(5)}\right]; \left[\overline{\boldsymbol{\sigma}}^{(6)}\right]\right] \tag{35}$$

where $\left[\overline{\boldsymbol{\sigma}}^{(i)}\right]$ is the macro stress in Voigt notation obtain for prescribed the macro strain $\overline{\boldsymbol{\epsilon}}^{(i)}$. The effective stiffness and effective compliance for studied cases are given in Table 1.

Table 1: Effective elastic constants in Voigt notation.

Effective stiffness	**Effective compliance**
Flat graphene	
$\overline{\mathbb{C}}_C = \begin{bmatrix} 43.3 & 18.7 & 8.77 & 0 & 0 & 0 \\ 18.7 & 43.3 & 8.77 & 0 & 0 & 0 \\ 8.77 & 8.77 & 14.1 & 0 & 0 & 0 \\ 0 & 0 & 0 & 0.079 & 0 & 0 \\ 0 & 0 & 0 & 0 & 0.079 & 0 \\ 0 & 0 & 0 & 0 & 0 & 12.3 \end{bmatrix}$ GPa	$\overline{\mathbb{S}} = \begin{bmatrix} 30.2 & -10.6 & -12.2 & 0 & 0 & 0 \\ -10.6 & 30.2 & -12.2 & 0 & 0 & 0 \\ -12.2 & -12.2 & 86.2 & 0 & 0 & 0 \\ 0 & 0 & 0 & 12700 & 0 & 0 \\ 0 & 0 & 0 & 0 & 12700 & 0 \\ 0 & 0 & 0 & 0 & 0 & 81.3 \end{bmatrix}$ MPa^{-1}
Flat graphene without interphase ($\mathbb{C}^I = \mathbb{C}^b$)	
$\overline{\mathbb{C}}_C = \begin{bmatrix} 42.6 & 18.2 & 8.77 & 0 & 0 & 0 \\ 18.2 & 42.6 & 8.77 & 0 & 0 & 0 \\ 8.77 & 8.77 & 13.2 & 0 & 0 & 0 \\ 0 & 0 & 0 & 0.079 & 0 & 0 \\ 0 & 0 & 0 & 0 & 0.079 & 0 \\ 0 & 0 & 0 & 0 & 0 & 12.2 \end{bmatrix}$ GPa	$\overline{\mathbb{S}} = \begin{bmatrix} 30.7 & -10.4 & -13.5 & 0 & 0 & 0 \\ -10.4 & 30.7 & -13.5 & 0 & 0 & 0 \\ -13.5 & -13.5 & 93.3 & 0 & 0 & 0 \\ 0 & 0 & 0 & 12700 & 0 & 0 \\ 0 & 0 & 0 & 0 & 12700 & 0 \\ 0 & 0 & 0 & 0 & 0 & 82.1 \end{bmatrix}$ MPa^{-1}
Flat graphene without interface ($\mathbf{K}^s \to \infty$)	
$\overline{\mathbb{C}}_C = \begin{bmatrix} 43.4 & 18.9 & 9.02 & 0 & 0 & 0 \\ 18.9 & 43.4 & 9.02 & 0 & 0 & 0 \\ 9.02 & 9.02 & 14.5 & 0 & 0 & 0 \\ 0 & 0 & 0 & 2.3 & 0 & 0 \\ 0 & 0 & 0 & 0 & 2.3 & 0 \\ 0 & 0 & 0 & 0 & 0 & 12.3 \end{bmatrix}$ GPa	$\overline{\mathbb{S}} = \begin{bmatrix} 30.2 & -10.6 & -12.2 & 0 & 0 & 0 \\ -10.6 & 30.2 & -12.2 & 0 & 0 & 0 \\ -12.2 & -12.2 & 84.3 & 0 & 0 & 0 \\ 0 & 0 & 0 & 435 & 0 & 0 \\ 0 & 0 & 0 & 0 & 435 & 0 \\ 0 & 0 & 0 & 0 & 0 & 81.3 \end{bmatrix}$ MPa^{-1}
Wrinkled graphene	
$\overline{\mathbb{C}}_C = \begin{bmatrix} 37.2 & 16.4 & 9.14 & 0 & 0 & 0 \\ 16.4 & 42.9 & 8.88 & 0 & 0 & 0 \\ 9.14 & 8.88 & 13.8 & 0 & 0 & 0 \\ 0 & 0 & 0 & 0.140 & 0 & 0 \\ 0 & 0 & 0 & 0 & 0.748 & 0 \\ 0 & 0 & 0 & 0 & 0 & 12.1 \end{bmatrix}$ GPa	$\overline{\mathbb{S}} = \begin{bmatrix} 35.4 & -10.0 & -17.0 & 0 & 0 & 0 \\ -10.0 & 29.8 & -12.5 & 0 & 0 & 0 \\ -17.0 & -12.5 & 91.8 & 0 & 0 & 0 \\ 0 & 0 & 0 & 7140 & 0 & 0 \\ 0 & 0 & 0 & 0 & 1340 & 0 \\ 0 & 0 & 0 & 0 & 0 & 82.6 \end{bmatrix}$ MPa^{-1}
Finite graphene	
$\overline{\mathbb{C}}_C = \begin{bmatrix} 31.5 & 14.9 & 8.79 & 0 & 0 & 0 \\ 14.9 & 39.4 & 8.79 & 0 & 0 & 0 \\ 8.79 & 8.79 & 14.1 & 0 & 0 & 0 \\ 0 & 0 & 0 & 0.773 & 0 & 0 \\ 0 & 0 & 0 & 0 & 1.13 & 0 \\ 0 & 0 & 0 & 0 & 0 & 8.69 \end{bmatrix}$ GPa	$\overline{\mathbb{S}} = \begin{bmatrix} 42.7 & -11.9 & -19.2 & 0 & 0 & 0 \\ -11.9 & 32.8 & -13.0 & 0 & 0 & 0 \\ -19.2 & -13.0 & 91.0 & 0 & 0 & 0 \\ 0 & 0 & 0 & 1290 & 0 & 0 \\ 0 & 0 & 0 & 0 & 885 & 0 \\ 0 & 0 & 0 & 0 & 0 & 115 \end{bmatrix}$ MPa^{-1}

5. Expression of Young's modulus as function of angle θ

For macroscopic tensile loading along direction $\mathbf{e}_t$, the macro stress tensor is :

$$\overline{\boldsymbol{\sigma}} = \sigma_t \mathbf{e}_t \otimes \mathbf{e}_t, \tag{36}$$

and the the macro strain tensor is given by

$$\overline{\boldsymbol{\epsilon}} = \overline{\mathbb{S}} : \overline{\boldsymbol{\sigma}} \tag{37}$$

where the fourth order tensor $\overline{\mathbb{S}} = \overline{\mathbb{C}}_{CM}^{-1}$ is the effective compliance tensor.

We define the effective Young's modulus associated to the tensile loading along direction $\mathbf{e}_t$ as

$$E(\mathbf{e}_t) = \frac{\sigma_t}{\epsilon_t} \tag{38}$$

where ϵ_t is the normal strain associated to the tensile loading along direction $\mathbf{e}_t$ defined by

$$\epsilon_t = \overline{\boldsymbol{\epsilon}} : \mathbf{e}_t \otimes \mathbf{e}_t. \tag{39}$$

In case of tensile loading along direction $\mathbf{e}_t = \cos(\theta)\,\mathbf{e}_1 + \sin(\theta)\,\mathbf{e}_3$, the macro stress tensor is

$$\overline{\boldsymbol{\sigma}} = \sigma_t \left[\cos^2(\theta)\,\mathbf{e}_1 \otimes \mathbf{e}_1 + \sin^2(\theta)\,\mathbf{e}_3 \otimes \mathbf{e}_3 + \cos(\theta)\sin(\theta)\,(\mathbf{e}_3 \otimes \mathbf{e}_1 + \mathbf{e}_1 \otimes \mathbf{e}_3)\right]. \tag{40}$$

Therefore, the macro stress and macro strain are in Voigt notation associated to the basis $(\mathbf{e}_1, \mathbf{e}_2, \mathbf{e}_3)$.

$$[\overline{\boldsymbol{\sigma}}] = \sigma_t \begin{bmatrix} \cos^2(\theta) \\ 0 \\ \sin^2(\theta) \\ 0 \\ \cos(\theta)\sin(\theta) \\ 0 \end{bmatrix}, \quad [\overline{\boldsymbol{\epsilon}}] = \left[\overline{\mathbb{S}}\right][\overline{\boldsymbol{\sigma}}] = \sigma_t \begin{bmatrix} \overline{\mathbb{S}}_{11}\cos^2(\theta) + \overline{\mathbb{S}}_{31}\sin^2(\theta) \\ \overline{\mathbb{S}}_{12}\cos^2(\theta) + \overline{\mathbb{S}}_{23}\sin^2(\theta) \\ \overline{\mathbb{S}}_{31}\sin^2(\theta) + \overline{\mathbb{S}}_{33}\cos^2(\theta) \\ 0 \\ \overline{\mathbb{S}}_{55}\cos(\theta)\sin(\theta) \\ 0 \end{bmatrix} \tag{41}$$

where $\overline{\mathbb{S}}_{ij}$ are effective compliance tensor components for transversally isotropic material. The macro strain can be rewritten as

$$\begin{aligned} \overline{\boldsymbol{\epsilon}} = {} & \sigma_t \left(\overline{\mathbb{S}}_{11}\cos^2(\theta) + \overline{\mathbb{S}}_{31}\sin^2(\theta)\right)\mathbf{e}_1 \otimes \mathbf{e}_1 \\ & + \sigma_t \left(\overline{\mathbb{S}}_{12}\cos^2(\theta) + \overline{\mathbb{S}}_{23}\sin^2(\theta)\right)\mathbf{e}_2 \otimes \mathbf{e}_2 \\ & + \sigma_t \left(\overline{\mathbb{S}}_{31}\sin^2(\theta) + \overline{\mathbb{S}}_{33}\cos^2(\theta)\right)\mathbf{e}_3 \otimes \mathbf{e}_3 \\ & + \sigma_t \frac{\overline{\mathbb{S}}_{55}\cos(\theta)\sin(\theta)}{2}\left(\mathbf{e}_3 \otimes \mathbf{e}_1 + \mathbf{e}_1 \otimes \mathbf{e}_3\right), \end{aligned}$$

and we deduce the normal strain ϵ_t

$$\begin{aligned}\epsilon_t &= \sigma_t \left(\overline{\mathbb{S}}_{11} \cos^2(\theta) + \overline{\mathbb{S}}_{31} \sin^2(\theta)\right) \cos^2(\theta) \\ &+ \sigma_t \left(\overline{\mathbb{S}}_{31} \sin^2(\theta) + \overline{\mathbb{S}}_{33} \cos^2(\theta)\right) \sin^2(\theta) \\ &+ \sigma_t \frac{\overline{\mathbb{S}}_{55}}{2} \left(\cos(\theta) \sin(\theta)\right)^2 .\end{aligned}$$

Finally, the effective Young's modulus $E(\theta)$ as function of the angle, θ, between the tensile direction and the vector $\mathbf{e}_1$ into the plane $(\mathbf{e}_1, \mathbf{e}_3)$ is

$$E(\theta) = \frac{1}{\overline{\mathbb{S}}_{11} \cos^4(\theta) + \overline{\mathbb{S}}_{33} \sin^4(\theta) + \left(2\overline{\mathbb{S}}_{31} + \frac{\overline{\mathbb{S}}_{55}}{2}\right) \sin^2(\theta) \cos^2(\theta)}. \tag{42}$$

References

[1] S. L. Mayo, B. D. Olafson, and W. A. Goddard. DREIDING: a generic force field for molecular simulations. *J. Phys. Chem.*, 94(26):8897–8909, 1990.

[2] J. P. Glusker, M. Lewis, and M. Rossi. *Crystal structure analysis for chemists and biologists*. John Wiley & Sons, 1994.

[3] D. N. Theodorou and U. W. Suter. Atomistic modeling of mechanical properties of polymeric glasses. *Macromolecules*, 19(1):139–154, 1986.

[4] Julien Yvonnet. *Computational homogenization of heterogeneous materials with finite elements*. Springer, 2019.

[5] Banafsheh Sajadi, Simon van Hemert, Behrouz Arash, Pierpaolo Belardinelli, Peter G Steeneken, and Farbod Alijani. Size-and temperature-dependent bending rigidity of graphene using modal analysis. *Carbon*, 139:334–341, 2018.